

A Realistic Pulsar – Supermassive Black Hole Timing Model

ZEXIN HU,^{1,2} ZIMING WANG,^{1,2} AND LIJING SHAO^{2,3}

¹*Department of Astronomy, School of Physics, Peking University, Beijing 100871, China*

²*Kawli Institute for Astronomy and Astrophysics, Peking University, Beijing 100871, China*

³*National Astronomical Observatories, Chinese Academy of Sciences, Beijing 100101, China*

ABSTRACT

Timing observation of pulsars orbiting around a supermassive black hole (SMBH) can measure the spacetime around the SMBH to a high precision and thus be a novel probe of the gravity theory. Future high-frequency surveys of the Galactic Centre (GC) region to be performed by the next-generation radio telescopes, such as the SKA, may discover pulsars that orbit around Sagittarius A* (Sgr A*), the SMBH dwelling in our GC. In this paper, we present a realistic pulsar-SMBH timing model based on the post-Newtonian equations of motion of the pulsar. Considering the expected timing precision in the future, we take into account several next-to-leading order light propagation time delays in the timing model. For the first time, we include the effects of proper motion of Sgr A*, which were expected to break the spin measurement degeneracy. We forecast the measurement precision of various parameters of Sgr A*, and discuss the data analysis procedure in the presence of red noise, which can be strong if the pulsar is a normal pulsar. The realistic timing model constructed in this study will serve as a useful tool in future searching and timing of pulsar-SMBH systems in the GC.

Keywords: Supermassive black holes (1663) — Pulsar timing method (1305) — Red noise (1956)

1. INTRODUCTION

Black holes (BHs) are one of the most fascinating objects predicted by General Relativity (GR), and measuring their fundamental properties can provide various tests of gravity theory in the strong-field region. Observations have revealed the existence of at least two types of astrophysical BHs, namely the stellar-mass BHs and the supermassive BHs (SMBHs). Since the first detection of gravitation waves (GWs) from a binary BH merger by the Advanced LIGO in 2015 (Abbott et al. 2016a), GW observations have provided hundreds of measurements of stellar-mass BHs (Abac et al. 2025a,b) and brought the tests of GR to high post-Newtonian (PN) orders (Abbott et al. 2016b). On the other hand, although it is believed that SMBHs exist at the center of most massive galaxies (McConnell & Ma 2013; Kormendy & Ho 2013), measuring their properties accurately remains a challenge. Current measurements of the spin of SMBHs mainly rely on the

spectroscopy (Reynolds 2014). But this method suffers from strong selection biases which favour high-spin BHs (Reynolds 2019), and can be unreliable for sources accreting near or above the Eddington rate (Riaz et al. 2020).

The SMBH in our Galaxy Centre (GC), Sagittarius A* (Sgr A*), is the closest SMBH to us. Monitoring the stars orbiting around it has provided a precise measurement of the mass of the SMBH, which is around $4.3 \times 10^6 M_{\odot}$, and its distance to the Solar System of about 8 kpc (Abuter et al. 2020). The detection of the Schwarzschild precession of the S2 orbit shows the appealing potential of testing gravity theory with Sgr A*. However, stars closer to Sgr A* need to be found for measuring the spin of the SMBH with astrometric observations (Waisberg et al. 2018), while the measurements come from the Event Horizon Telescope (EHT) observations of Sgr A* currently can only loosely suggest a moderate to large spin magnitude (Akiyama et al. 2022, 2024).

Timing pulsars orbiting around Sgr A* can be a novel probe of the SMBH properties (Wex & Kopeikin 1999; Pfahl & Loeb 2004; Liu et al. 2012; Psaltis et al. 2016; Zhang & Saha 2017; Hu et al. 2023; Hu & Shao 2024;

Shao & Hu 2025), as well as theories of gravity (Dong et al. 2022; Hu et al. 2024b). Previous studies have shown that timing one pulsar with an orbital period less than ~ 0.5 yr or combining the timing of two pulsars with orbital periods less than ~ 5 yr can both measure the spin of Sgr A* to better than 1% level (Liu et al. 2012; Hu & Shao 2024). Further, timing a pulsar with a tight orbit can even measure the quadrupole moment of Sgr A* (Wex & Kopeikin 1999), which provides a test of the no-hair theorem in GR (Carter 1971).

Current surveys have not found any close pulsars orbiting around Sgr A* yet. In fact, there are only several pulsars that have been found in the GC region (Deneva et al. 2009; Johnston et al. 2006; Eatough et al. 2013; Rea et al. 2013; Lower et al. 2024; Abbate et al. 2025), much fewer than the expected population of pulsars there. The “missing pulsar problem” may be partially caused by the complex interstellar medium (ISM) environment in the GC region, which makes the detection a challenge for observations at the typical low frequencies (Cordes & Lazio 2002), while high-frequency surveys at the current stage are limited by the steep spectrum of the pulsar emission and the instrument sensitivity. Astrophysical explanation considering the formation and evolution of pulsars at the GC may also account for the absence of pulsars (Dexter & O’Leary 2014). Nevertheless, future observations with next-generation radio telescopes are still possible to find pulsars in the GC and even close pulsars orbiting around Sgr A* (Liu et al. 2012; Bower et al. 2018; Desvignes et al. 2026).

The upcoming opportunities of finding and timing pulsars orbiting around Sgr A* demand the development of a realistic timing model that can be used in real data analysis for the very special pulsar-SMBH system. The so-called timing model describes the relation between the times of arrival (TOAs) of pulsar pulses observed at the Earth telescopes and the proper rotation of the pulsar in its own inertial frame (Damour & Deruelle 1986; Hu et al. 2024a). Due to the orbital motion of the pulsar as well as the curved spacetime caused by the SMBH, the pulses observed on Earth are not simply periodic signals. A comparison between the model prediction and observed TOAs will enable the measurement of system parameters.

The timing model for the pulsar-SMBH system is significantly different from those models used for currently timed binary pulsars, mainly due to the grand mass of the SMBH. The large orbital semi-major axis of the pulsar in the pulsar-SMBH system leads to leading-order time delays at the order of 10^4 s for a pulsar with an orbital period $P_b \sim 0.5$ yr (Hu et al. 2023). The large time delays enable the detection of next-to-leading-order

(NLO) effects in this system. Besides, the angular momentum of the system is dominated by the spin of the SMBH, thus the spin-orbit coupling is important in this system (Wex & Kopeikin 1999). Many high-order effects that just begin to be measured in the Double Pulsar system (Kramer et al. 2021) should be easily detectable in a pulsar-SMBH system and therefore need to be taken into account for a realistic timing model.

Currently, the development of the pulsar-SMBH timing model is mainly based on the analytic solution of the second-order PN motion of compact binary systems with spin, derived by Wex (1995), and incorporation of the quadrupole effects of the SMBH perturbatively (Liu et al. 2012; Psaltis et al. 2016). The analytic timing model takes the key advantage of a parametrized approach, which can be partially theory independent (Damour & Taylor 1992). It is also computationally cheap compared to, for example, a full GR model (see e.g., Zhang & Saha 2017). However, the analytical timing model is relatively hard to describe additional effects come from various perturbations such as the astrophysical environment around Sgr A* (see e.g., Hu et al. 2023, for perturbations from dark matter) or corrections from modified gravity theories (Dong et al. 2022; Hu et al. 2024b), especially for those periodic effects that deform the pulsar orbit from an ellipse.

In this paper, we aim to provide a comprehensive description of a realistic numerical timing model based on previous developments in Hu et al. (2023). We here further complete the timing model by incorporating all detectable high-order effects, so that the timing model provided in this paper can be applied to real data analysis. We also give a detailed discussion on the parameter estimation procedure based on the numerical timing model and mock data simulations. Particularly, we study the parameter estimation in the presence of red noise, which can be important in the pulsar-SMBH system for a normal pulsar (instead of a millisecond pulsar). This is usually expected after taking the scattering effects of pulsar pulses with the interstellar medium into consideration (Abbate et al. 2025).

The remaining part of this paper is organized as follows. In Section 2 we describe the details of the realistic pulsar-SMBH timing model. In Section 3, we forecast the expected measurement precision of the SMBH properties for future observation. We discuss the data analysis procedure in the presence of red noise in Section 4. Section 5 summarizes our results.

2. TIMING MODEL

A pulsar timing model describes the relation between the observed TOAs of pulsar pulses and the

stable proper rotation of the pulsar in its inertial frame (Damour & Deruelle 1986), which is an essential part for timing data analysis. In this section, we focus only on the timing model for the pulsar-SMBH system, which describes the TOAs at the Solar System Barycenter (SSB) and of infinite frequency. We first describe the propagation of the radio signal in the curved SMBH spacetime in Section 2.1, followed by the orbital dynamics of the pulsar in Section 2.2. A complete description of the timing model is shown in Section 2.3. In Section 2.4, we construct an efficient inverse timing model for real data analysis. As an overview, we summarize various effects considered in the pulsar orbital motion in Table 1, and give a fiducial case study of pulsar orbits and time delays in Figure 1 and Figure 2, respectively.

2.1. Light propagation

A radio pulse signal emitted by a pulsar needs to travel through the curved spacetime of the SMBH before it arrives at the telescopes on Earth. In the pulsar timing procedure, various time delays are used to describe this process. At the leading order, the time for light to travel through the flat spacetime is accounted by the so-called Römer delay

$$\Delta_{\text{R}} = \frac{1}{c} \mathbf{r} \cdot \hat{\mathbf{K}}_0 = \frac{z}{c}, \quad (1)$$

where \mathbf{r} is the relative position vector pointing from the SMBH to the pulsar, $\hat{\mathbf{K}}_0$ is the unit vector of the line of sight direction, and $z \equiv \mathbf{r} \cdot \hat{\mathbf{K}}_0$. A time shift corresponding to the distance d between the Sgr A* and SSB is subtracted from the expression, which, in the constant case, is only a matter of redefinition of the reference time epoch. The effects caused by the relative motion between the SSB and Sgr A* are discussed in Section 2.3.

The lowest-order propagation time delay caused by the spacetime curvature of the pulsar companion is also well studied and can be measured in many binary pulsar systems (Manchester et al. 2005; Freire & Wex 2024). It is described by the 1PN Shapiro delay (Shapiro 1964; Blandford & Teukolsky 1976),

$$\Delta_{\text{S1}} = -\frac{2GM}{c^3} \ln(r - z), \quad (2)$$

where M is the mass of the SMBH and $r = |\mathbf{r}|$. A constant term is again subtracted from the expression, assuming that the distance between Sgr A* and SSB tends to infinity, which is reasonable when considering the PN effects. One should notice that the splitting of Römer delay and Shapiro delay as above is a coordinate-dependent concept (Damour & Taylor 1992), and in this

paper, we always work in the harmonic coordinates centered on the SMBH.

Although in current pulsar timing observations, the NLO effects caused by higher PN corrections to the light propagation have only started to be observed in a limited number of systems, for example, in the Double Pulsar system (Kramer et al. 2021), a rough estimation suggests that the 2PN Shapiro delay should be observable for the pulsar-SMBH system. For a pulsar in a circular orbit with an orbital period $P_b = 1$ yr and a moderate orbital inclination $i = 30^\circ$, the amplitude of the 1PN Shapiro delay can be estimated by Equation (2),

$$\Delta_{\text{S1}} \sim \frac{2GM}{c^3} \ln \frac{1 + \sin i}{1 - \sin i} \sim 50 \text{ s}. \quad (3)$$

The 2PN Shapiro delay should roughly have an amplitude at the order of $\beta_O^2 \times 50 \text{ s} \sim 10 \text{ ms}$, where the characteristic orbital velocity parameter is

$$\beta_O = \frac{(GMn_b)^{1/3}}{c}, \quad (4)$$

with $n_b \equiv 2\pi/P_b$ (Damour & Taylor 1992). The exact amplitude of the 2PN effects can be even larger for orbits with large eccentricity and inclination angles closer to 90° .

The expected timing precision of GC pulsars for future next-generation telescopes such as the SKA is expected to reach at least $\sigma_{\text{TOA}} = 1 \text{ ms}$ (Liu et al. 2012). Thus, the 2PN Shapiro delay should be taken into account in the pulsar-SMBH timing model. The analytic expression of the 2PN Shapiro delay in the harmonic coordinates is given by Klioner & Zschocke (2010),

$$\Delta_{\text{S2}} = \Delta_{\Delta\text{PN}} + \Delta_{\text{PPN}}, \quad (5)$$

where

$$\Delta_{\Delta\text{PN}} = -\frac{4G^2M^2}{c^5r} \left(1 - \frac{z}{r}\right)^{-1}, \quad (6)$$

and

$$\Delta_{\text{PPN}} = -\frac{G^2M^2}{4c^5r} \left(\frac{z}{r} - 15 \frac{\arccos(-z/r)}{\sqrt{1 - z^2/r^2}} \right), \quad (7)$$

with the range of the arccosine function $[0, \pi]$. In these expressions, we have again taken the distance between the Sgr A* and SSB to infinity.

For the Double Pulsar system, the 2PN Shapiro delay is taken into account in an elegant way, which can be written as

$$\Delta_{\text{S}} = \Delta_{\text{S1}} + \Delta_{\text{S2}} = -2r \ln(\Lambda_u + \delta\Lambda_u^{\text{len}}). \quad (8)$$

Here, r is the so-called range parameter instead of the distance between the pulsar and SMBH. The detailed

definition of r , Λ_u and $\delta\Lambda_u^{\text{len}}$ can be found in Kramer et al. (2021). This simplified expression is based on the fact that the term Δ_{PPN} is bounded as (Klioner & Zschocke 2010)

$$|\Delta_{\text{PPN}}| \leq \frac{15}{4} \pi \frac{G^2 M^2}{c^5 d_i}, \quad (9)$$

where d_i is the impact parameter for the light travel in a straight line. For the Double Pulsar system, taking d_i as the radius of a neutron star, and M to be at the order of one Solar mass, this gives an upper bound $\sim 20 \mu\text{s}$, which is below the timing precision and can be safely ignored (Kramer et al. 2021). However, for the pulsar-SMBH system, this bound is not small enough as it gives a value as large as the 1PN effect. Our simulations also show that Δ_{PPN} can be the same order of, or even larger than, Δ_{PN} for the pulsar-SMBH system, so that we need to take both of them into account.

A simple estimation of the amplitude of the 2PN Shapiro delay and the future conservatively-estimated timing precision for GC pulsars in fact suggests that Shapiro delay at even higher PN orders might be detectable for a pulsar-SMBH system with a small orbital period, large orbital eccentricity and nearly edge-on inclination, though the probability for finding such pulsars might be rather low for future observations. Here we stop at the 2PN level, and higher-order contributions, if necessary, can be added in a similar manner.

The above discussions have not considered the spin of the SMBH. The Shapiro delay describes the additional light propagation time in the Schwarzschild spacetime, while the spin of the SMBH leads to the so-called frame-dragging effect (Lense & Thirring 1918; Wex & Kopeikin 1999). For the pulsar-SMBH system, the leading-order time delay caused by the frame-dragging effect is effectively at the 2PN order and is (Wex & Kopeikin 1999),

$$\Delta_{\text{FD}} = -\chi \frac{2G^2 M^2}{c^5} \frac{\hat{\mathbf{s}} \cdot (\hat{\mathbf{K}}_0 \times \hat{\mathbf{n}})}{r - z}, \quad (10)$$

where $\hat{\mathbf{n}} \equiv \mathbf{r}/r$, $\hat{\mathbf{s}} \equiv \mathbf{S}/S$, and $\chi = cS/GM^2$ is the dimensionless spin of the SMBH.

Now we have listed out all the time delays corresponding to light propagation in the curved spacetime of the SMBH, consistent to the 2PN order. Higher-order effects can be added similarly if necessary. We should mention that analytic solutions for null geodesics in the Schwarzschild or Kerr spacetime can be expressed with various kinds of elliptic functions and parametrized by the constants of motion (Hackmann & Dhani 2019; Cieřlik et al. 2023). One can then numerically solve the so-called emitter-observer problem to get the time

delays for light propagation. This procedure automatically takes into account full GR effects. However, we choose to use the expanded formulas introduced in this subsection, as they are computationally cheaper, easier to extend for astrophysical perturbations or gravity theories beyond GR, and they are very convenient for the construction of the inverse timing model in Section 2.4.

Finally, as mentioned at the beginning, we ignore the various effects caused by the ISM, such as dispersion or scattering (Lorimer & Kramer 2005). These effects are expected to be frequency-dependent and might be removed with multi-frequency observation.

2.2. Orbital dynamics

For our purpose to build a timing model that can be applied in future data analysis, we first treat the pulsar as a test particle moving in the spacetime of the central SMBH. We use the 2PN equations of motion and keep the leading-order effects of the spin-orbital coupling and the SMBH quadrupole moment (Hu et al. 2023). The equations of motion of the pulsar in the harmonic coordinates read,

$$\ddot{\mathbf{r}} = \ddot{\mathbf{r}}_{\text{N}} + \ddot{\mathbf{r}}_{\text{1PN}} + \ddot{\mathbf{r}}_{\text{SO}} + \ddot{\mathbf{r}}_{\text{Q}} + \ddot{\mathbf{r}}_{\text{2PN}}, \quad (11)$$

where dots denote the derivative with respect to the coordinate time t . Besides the Newtonian acceleration, $\ddot{\mathbf{r}}_{\text{N}} = -GM\hat{\mathbf{n}}/r^2$, other terms in Equation (11) represent the 1PN and 2PN corrections and the leading-order contributions from the SMBH spin and quadrupole moment. Their expressions are (Barker & O'Connell 1975; Damour & Schaefer 1988),

$$\ddot{\mathbf{r}}_{\text{1PN}} = -\frac{GM}{c^2 r^2} \left[\left(-\frac{4GM}{r} + v^2 \right) \hat{\mathbf{n}} - 4\dot{r}\mathbf{v} \right], \quad (12a)$$

$$\ddot{\mathbf{r}}_{\text{SO}} = \chi \frac{6G^2 M^2}{c^3 r^3} \left[\hat{\mathbf{s}} \cdot (\hat{\mathbf{n}} \times \mathbf{v}) \hat{\mathbf{n}} + \dot{r} (\hat{\mathbf{n}} \times \hat{\mathbf{s}}) - \frac{2}{3} (\mathbf{v} \times \hat{\mathbf{s}}) \right], \quad (12b)$$

$$\ddot{\mathbf{r}}_{\text{Q}} = -q \frac{3G^3 M^3}{2c^4 r^4} \left\{ \left[5 (\hat{\mathbf{n}} \cdot \hat{\mathbf{s}})^2 - 1 \right] \hat{\mathbf{n}} - 2 (\hat{\mathbf{n}} \cdot \hat{\mathbf{s}}) \hat{\mathbf{s}} \right\}, \quad (12c)$$

$$\ddot{\mathbf{r}}_{\text{2PN}} = \frac{G^2 M^2}{c^4 r^3} \left[\left(2\dot{r}^2 - \frac{9GM}{r} \right) \hat{\mathbf{n}} - 2\dot{r}\mathbf{v} \right], \quad (12d)$$

where $\mathbf{v} = \dot{\mathbf{r}}$ and $v = |\mathbf{v}|$. Similar to the spin, $q \equiv c^4 Q/G^2 M^3$ is the dimensionless quadrupole moment of the SMBH, with Q the (dimensionful) quadrupole moment. By writing down the above equations, we have made several assumptions and simplifications to the orbital motion of the pulsar, and we justify these assumptions as follows.

In above equations, we have assumed that the spacetime of the SMBH is axisymmetric, like the Kerr spacetime. But we do not impose the constraint from the no-hair theorem, which states that the spacetime of a Kerr BH is fully determined by the BH mass and spin, and thus the dimensionless quadrupole moment q depends on the dimensionless spin parameter χ via $q = -\chi^2$ (Thorne 1980). The independent treatment of χ and q is especially convenient when one is aiming to test the no-hair theorem, as this timing model can provide an independent measurement of the two parameters.

In Equations (11) and (12), we have neglected the finite mass ratio of the pulsar and SMBH, which is at the order of $m_{\text{PSR}}/M \lesssim 10^{-6}$. At the Newtonian order, this only leads to an effective (mis)identification of the SMBH mass M to be $M + m_{\text{PSR}}$. Even though the theoretical estimation of the SMBH mass measurement precision in such a pulsar-SMBH system can reach a relative error of 10^{-6} or better for a pulsar with a very small orbital period, $P_b \lesssim 0.1$ yr (Liu et al. 2012; Hu et al. 2023), it seems unrealistic to have such a precise measurement of the SMBH mass in practice due to the complex astrophysical environment around Sgr A*. This simple argument then suggests that the effects caused by the finite mass ratio are likely to be unobservable in the near future, considering the probability of finding such a close pulsar and the lack of detailed modeling of other environmental perturbations. Therefore, we ignore all corrections corresponding to the small mass ratio.

For the term $\ddot{\mathbf{r}}_{\text{SO}}$ shown in Equation (12b), we have not specified a spin supplementary condition (SSC), which corresponds to the ambiguity of choosing the representation point for spinning objects in GR (Barker & O’Connell 1974). Though the detailed expression of the spin-orbit coupling term depends on the choice of SSC, they only introduce a fractional change at the order of the mass ratio m_{PSR}/M for compact objects like neutron stars (Kidder 1995; Li et al. 2024), and thus it can be ignored in our calculation. From another estimation, different SSCs will introduce a shift of the representation point of the pulsar at the order of $vS_{\text{PSR}}/m_{\text{PSR}}c^2$ (Barker & O’Connell 1974), which gives a time delay at the order of $0.1 \mu\text{s}$ for a millisecond pulsar with an orbital period ~ 1 yr. This is far below the expected timing precision and thus is negligible. Also, we ignore the spin-orbit coupling term contributed by the pulsar’s spin and the spin-spin coupling, as the spin of pulsar in the system is much smaller than that of the SMBH (Wex & Kopeikin 1999).

We truncate the expansion of equations of motion (11) at the 2PN level, as the higher-order contributions can

be shown to be negligible for the expected timing precision of the SKA and realistic observation time spans. The higher-order PN corrections can be separated into two parts: one is the conservative part starting from the 3PN level, which is similar to what we have included in the current equations, and the other one is the back reaction of the GW radiation starting from the 2.5PN level and it is proportional to the small mass ratio. For the 3PN corrections, it will deform the orbit, leading to a periodic effect at the order of $\beta_0^6 \times \Delta_R \sim 1 \mu\text{s} (P_b/1 \text{ yr})^{-4/3}$, which is too small to be detected. At the same time, it will also cause an additional periastron advance with $\dot{\omega}^{3\text{PN}} \sim \beta_0^4 \dot{\omega}^{1\text{PN}}$, where ω is the longitude of the periastron and $\dot{\omega}^{1\text{PN}} = 3GMn_b/c^2 a(1 - e^2)$ with a and e the semi-major axis and eccentricity of the pulsar orbit respectively (Damour & Deruelle 1986). Though the orbital eccentricity may further amplify $\dot{\omega}^{3\text{PN}}$, for orbits with moderate eccentricity, we may roughly account for the effects of eccentricity to a factor of 10 and can estimate the time delay caused by the secular effect to be

$$\dot{\omega}^{3\text{PN}} T_{\text{obs}} a \sin i / c \sim 1 \text{ ms} \left(\frac{T_{\text{obs}}}{5 \text{ yr}} \right) \left(\frac{P_b}{1 \text{ yr}} \right)^{-7/3} \sin i, \quad (13)$$

with T_{obs} the total observing time span. Having said that, similar to the higher-order terms of the Shapiro delay, the estimation in fact suggests that for pulsar-SMBH systems with small P_b , large e , and a nearly edge-on inclination, also with a large T_{obs} or a better timing precision, the secular effect of 3PN corrections might be observable. However, a similar argument as for ignoring the mass ratio also applies to the 3PN corrections, as the secular effects caused by PN corrections are largely degenerate with the secular effects caused by the environmental perturbations, and it seems impractical to model the environmental effects to such a high precision. This is different when considering secular effects, as they can have distinctive signatures and be separated.

The dissipative 2.5PN correction will cause a decay of the pulsar orbit, which provided the first evidence for the existence of GWs in the binary pulsar system PSR B1913+16 (Taylor et al. 1979). The leading-order change rate of the pulsar orbital period caused by GW emission can be expressed as (Peters & Mathews 1963; Poisson & Will 2014),

$$\dot{P}_b = -\frac{192\pi}{5} \frac{m_{\text{PSR}}}{M} f(e) \beta_0^5, \quad (14)$$

with

$$f(e) = (1 - e^2)^{-7/2} \left(1 + \frac{73}{24} e^2 + \frac{37}{96} e^4 \right). \quad (15)$$

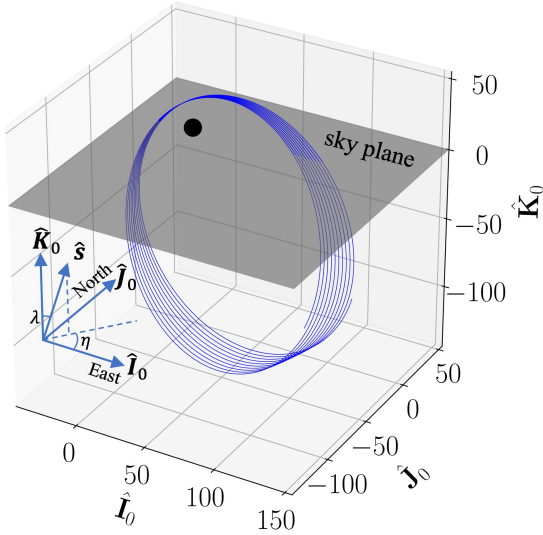


Figure 1. Illustration of the pulsar orbit with system parameters given in Equation (17). The axes are in the unit of AU.

For a pulsar in a pulsar-SMBH system with an orbital period $P_b = 1$ yr and orbital eccentricity $e = 0.8$, one has $\dot{P}_b \sim -5 \times 10^{-12}$. This leads to a cumulated time delay at the order of

$$\pi \dot{P}_b \frac{T^2}{P_b^2} \frac{a \sin i}{c} \sim 30 \mu\text{s} \left(\frac{T_{\text{obs}}}{5 \text{ yr}} \right)^2 \left(\frac{P_b}{1 \text{ yr}} \right)^{-3} \sin i. \quad (16)$$

Therefore, for a total observation time span at the order of 10 yr, it is not necessary to consider the orbital decay caused by GWs, while such an observation time span already permits a precise measurement of the SMBH spin and quadrupole moment (Liu et al. 2012; Hu et al. 2023).

Finally, as mentioned before, various environmental perturbations also affect the orbital motion of the pulsar. For example, Merritt et al. (2010) studied the effects of stellar mass objects in the context of using stellar orbits to measure the SMBH properties. Hu et al. (2023) have studied the effects caused by dark matter spike around the SMBH. It is interesting and important to study how to model the environmental effects in our GC and how they will affect the timing observations, though it is beyond the scope of this work and we leave it for future study.

The above discussions justify the validity of using Equations (11) and (12) to describe the pulsar orbital motion for our timing model. As a fiducial case, in Figure 1, we illustrate the orbit of a pulsar for a total time

span $T_{\text{obs}} = 5$ yr in a system with the following parameters,

$$M = 4.3 \times 10^6 M_{\odot}, \quad (17a)$$

$$\chi = 0.6, \quad \lambda = \frac{\pi}{6}, \quad \eta = \frac{5\pi}{9}, \quad q = -0.36, \quad (17b)$$

$$P_b = 0.5 \text{ yr}, \quad e = 0.8, \quad (17c)$$

$$i = \frac{\pi}{5}, \quad \omega = \frac{5\pi}{7}, \quad \Omega = 0, \quad f_0 = -\frac{3\pi}{4}, \quad (17d)$$

where λ and η describe the direction of the SMBH spin relative to the coordinate frame $(\hat{I}_0, \hat{J}_0, \hat{K}_0)$ with \hat{I}_0, \hat{J}_0 pointing towards east and north respectively. Then we have $\hat{s} = (\sin \lambda \cos \eta, \sin \lambda \sin \eta, \cos \lambda)$, as shown in the figure. Parameters in $\Theta_{\text{orb}} = \{P_b, e, i, \omega, \Omega, f_0\}$ are the usual orbital elements describing a Keplerian orbit (Poisson & Will 2014), and some of them have been defined before except that Ω is the longitude of the ascending node and f_0 is the initial orbital true anomaly. The values of the SMBH parameters $\Theta_{\text{SMBH}} = \{M, \chi, \lambda, \eta, q\}$ are inspired by results from Abuter et al. (2020) and Akiyama et al. (2024), where the former gives an accurate measurement of the SMBH mass and the latter suggests a moderate to large spin with a small inclination.¹ Here, we use a moderate value for the dimensionless spin, so that it may represent a conservative case for estimating the spin measurement precision. The angles for the orbital parameters are randomly chosen to avoid special orientations that might render the parameter-estimation problem degenerate. Because of the PN correction, the orbit of the pulsar in fact is not a Keplerian orbit. Thus, one should regard the orbital parameters in the sense of osculating elements of the orbit at a reference time. They are equivalent to the initial position and velocity vectors of the pulsar (Poisson & Will 2014).

Before ending this subsection, we want to discuss the spin evolution of the pulsar. Due to the curved space-time of the SMBH, the rotation axis of the pulsar suffers a precession. At the leading order, the precession of the spin of the pulsar can be written as (Barker & O'Connell 1979)

$$\frac{d\hat{e}_3}{dt} = (\boldsymbol{\Omega}_{\text{DS}} + \boldsymbol{\Omega}_{\text{LT}}) \times \hat{e}_3, \quad (18)$$

where \hat{e}_3 is the direction of the spin axis of the pulsar in the center of mass frame, the one where we describe the pulsar's orbital motion. Geodesics precession and

¹ Note that there is a sign difference in the definition of the line of sight.

Table 1. Approximate time delays related to different effects in the pulsar’s orbital motion. The second column gives an order-of-magnitude estimation for the time delays caused by different effects, while the last column shows if the effect is included in our timing model. Except for the Newtonian term related to the Keplerian orbit, we estimate the cumulative time delays caused by secular effects. The third column shows the estimation results for the fiducial system with system parameters in equations (17). For terms including the mass ratio m_{PSR}/M , m_{PSR} is taken to be $1.4 M_{\odot}$, and for the SSC term we take the rotation period of the pulsar to be 1 ms. Dimensionless $P_{b1} \equiv P_b/(1 \text{ yr})$ and $T_{\text{obs}1} \equiv T_{\text{obs}}/(1 \text{ yr})$ are respectively P_b and T_{obs} in unit of year. Note that the dependence on orbital parameters in the second column is not complete and can only serve as a reference.

Effects	Time Delay [s]	Time Delay (fiducial) [s]	Included
Newtonian	$8 \times 10^4 P_{b1}^{2/3} \sin i$	3×10^4	Yes
1PN	$4 \times 10^2 P_{b1}^{-1} T_{\text{obs}1} (1 - e^2)^{-1} \sin i$	7×10^3	Yes
Spin-orbit coupling	$4 \chi P_{b1}^{-4/3} T_{\text{obs}1} (1 - e^2)^{-3/2} \sin i$	80	Yes
2PN	$0.7 P_{b1}^{-5/3} T_{\text{obs}1} (1 - e^2)^{-2} \sin i$	50	Yes
Quadrupole	$0.03 q P_{b1}^{-5/3} T_{\text{obs}1} (1 - e^2)^{-2} \sin i$	1	Yes
Mass ratio	$3 \times 10^{-2} P_{b1}^{2/3} \sin i$	1×10^{-2}	No
Radiation reaction	$6 \times 10^{-9} P_{b1}^{-3} T_{\text{obs}1}^2 (1 - e^2)^{-7/2} f(e) \sin i$	1×10^{-4}	No
Higher PN	$2 \times 10^{-4} P_{b1}^{-7/3} T_{\text{obs}1} \sin i$	3×10^{-3}	No
SSC	$2 \times 10^{-7} P_{b1}^{-1/3}$	2×10^{-7}	No

Lense-Thirring precession are

$$\boldsymbol{\Omega}_{\text{DS}} = \frac{3 GM}{2 c^2 r^3} \mathbf{r} \times \mathbf{v}, \quad (19)$$

$$\boldsymbol{\Omega}_{\text{LT}} = \chi \frac{G^2 M^2}{c^3 r^3} [3(\hat{\mathbf{n}} \cdot \hat{\mathbf{s}})\hat{\mathbf{n}} - \hat{\mathbf{s}}], \quad (20)$$

respectively. For a pulsar in a circular, $P_b = 1 \text{ yr}$ orbit, the precession rate caused by them are $|\boldsymbol{\Omega}_{\text{DS}}| \sim 0.1 \text{ deg yr}^{-1}$ and $|\boldsymbol{\Omega}_{\text{LT}}| \sim 10^{-3} \text{ deg yr}^{-1}$. The precession rate in the pulsar-SMBH system is rather low compared to the rate in compact binary pulsar systems (Kramer et al. 2021) as the spacetime curvature here is in fact smaller. Such a small precession rate seems sub-dominant in near future observations, and we take $\hat{\mathbf{e}}_3$ as a constant direction in our analysis.

As a short summary and for useful references, we conclude all the effects discussed in Table 1.

2.3. The pulsar-SMBH timing model

With the pulsar’s orbital motion and light propagation in the SMBH spacetime described before, we can build the timing model that predicts the TOAs of pulsar pulses. The pulsar rotates extremely stably in its own inertial frame. Therefore, the rotation of the pulsar can be described by (Damour & Deruelle 1986)

$$N(T) = N_0 + \nu T + \frac{1}{2} \dot{\nu} T^2 + \dots, \quad (21)$$

where T is the proper time of the pulsar, N is the proper rotation number, N_0 is a constant for initial condition, ν is the rotation frequency of the pulsar and $\dot{\nu}$ describes the spin-down of the pulsar. Note that, only here, the dot in fact denotes a derivative with respect to T . In our model, we ignore the glitches of the pulsar, as large glitches can be recovered and dealt with in later data analysis, while small glitches will be likely counted as timing red noise discussed in the later section.

We may regard the emission time of the pulsar pulse to be the time that the pulsar rotated to a specific direction and its emission beam is pointing to the Earth. Without losing generality, we can choose it to be the time that N is an integer (Damour & Deruelle 1986), then Equation (21) gives the emission time of the N -th pulse. However, the orbital motion of the pulsar leads to an aberration effect that in fact changes the exact rotation phase of the pulsar when the pulsar emission beam points to the Earth, and this can be accounted for by the so-called aberration delay (Damour & Deruelle 1986)

$$\Delta_{\text{A1}} = -\frac{1}{2\pi\nu} \frac{\mathbf{v} \cdot (\hat{\mathbf{K}}_0 \times \hat{\mathbf{e}}_3)}{c |\hat{\mathbf{K}}_0 \times \hat{\mathbf{e}}_3|^2}, \quad (22)$$

where a term proportional to r/d is ignored as the distance between Sgr A* and SSB is large enough. For a pulsar with its spin aligned with the orbital angular momentum, the amplitude of the leading-order aberration

delay is at the order of

$$\Delta_{A1} \sim 3 \text{ ms} \left(\frac{\nu}{1 \text{ Hz}} \right)^{-1} \left(\frac{P_b}{1 \text{ yr}} \right)^{-1/3} \sin^{-1} i, \quad (23)$$

which suggests that the aberration delay should be taken into account for a pulsar-SMBH system, especially if a normal pulsar is observed. In fact, the next-order aberration delay only becomes smaller by a factor of $v/c \sim 10^{-1} - 10^{-2}$ and thus might be relevant for a normal pulsar or a pulsar in a tight orbit. In Appendix A, we give a calculation of the next-order aberration delay caused by the pulsar's motion, and it is expressed as

$$\Delta_{A2} = \Delta_{A1} \left(\frac{\mathbf{v} \cdot \hat{\mathbf{K}}_0}{2c} + \frac{\mathbf{v} \cdot [\hat{\mathbf{K}}_0 - (\hat{\mathbf{K}}_0 \cdot \hat{\mathbf{e}}_3)\hat{\mathbf{e}}_3]}{c|\hat{\mathbf{K}}_0 \times \hat{\mathbf{e}}_3|^2} \right). \quad (24)$$

Though the timing precision for normal pulsars is, in general, worse than that for millisecond pulsars, we add this term to our timing model as it can be relevant for pulsars in relativistic and eccentric orbits.

We remind here that the aberration, as well as the lensing of the light to be discussed later, will also effectively change the line of sight direction for the pulsar, which means that we will observe a different part of the emission region as a function of time (Damour & Taylor 1992). This latitudinal aberration effect has been observed in, for example, PSR B1534+12 (Stairs et al. 2004). In the pulsar-SMBH system, the line of sight variation at the leading order is (Damour & Taylor 1992)

$$\delta\zeta = - \left(\hat{\mathbf{K}}_0 \times \frac{\mathbf{v}}{c} \right) \cdot \frac{\hat{\mathbf{e}}_3 \times \hat{\mathbf{K}}_0}{|\hat{\mathbf{e}}_3 \times \hat{\mathbf{K}}_0|}, \quad (25)$$

which is about 1° for a pulsar with $P_b = 1 \text{ yr}$. Depending on the real situation, the variation of the pulse profile may or may not need to be taken into account for a better determination of TOAs. Here, we ignore the latitudinal effect as it relates to the modeling of the pulsar emission region that varies for different pulsars.

The above aberration delay fully comes from special-relativistic effects in the flat spacetime. The deflection of the pulsar's signal caused by the SMBH leads to a lensing correction to the aberration delay (Doroshenko & Kopeikin 1995)

$$\Delta_L = \frac{1}{2\pi\nu} \frac{2GM}{c^2} \frac{\hat{\mathbf{n}}}{r-z} \cdot \frac{\hat{\mathbf{K}}_0 \times \hat{\mathbf{e}}_3}{|\hat{\mathbf{K}}_0 \times \hat{\mathbf{e}}_3|^2}, \quad (26)$$

which is proportional to the mass of SMBH. For a pulsar that spins aligned with the orbital angular momentum, the term is at the order of $\sim 0.3 \text{ ms}$ for a pulsar with $\nu = 1 \text{ Hz}$, $P_b = 1 \text{ yr}$, and a moderate orbital inclination.

Although the mass of SMBH is very large compared to the usual companion in a binary pulsar system, the lensing correction still only becomes important for systems close to edge-on. Nevertheless, we include this correction in our timing model.

Counting into the aberration delay, the emission time T_e of a pulse in the pulsar's proper frame is given by

$$T_e = T + \Delta_{A1} + \Delta_{A2} + \Delta_L. \quad (27)$$

We note that the quantities in the aberration delay, such as \mathbf{r} and \mathbf{v} , in principle should take their values at time T_e , which is the time when the pulse is emitted. However, changing to their values at T only introduces a fractional change at the order of Δ_A/P_b , which can be safely ignored.

The proper time T of the pulsar is related to the coordinate time t via

$$\begin{aligned} \frac{dT}{dt} \simeq 1 - \frac{GM}{rc^2} - \frac{1}{2} \frac{v^2}{c^2} + \frac{1}{2} \left(\frac{GM}{rc^2} \right)^2 \\ - \frac{3}{2} \frac{GM}{rc^2} \frac{v^2}{c^2} - \frac{1}{8} \frac{v^4}{c^4}, \end{aligned} \quad (28)$$

accurate to the 2PN order (Wex 1995). The spin contribution of the SMBH,

$$\left(\frac{dT}{dt} \right)_S = \chi \frac{2G^2 M^2}{c^5 r^2} \hat{\mathbf{s}} \cdot (\hat{\mathbf{n}} \times \mathbf{v}), \quad (29)$$

is ignored to be consistent with our 2PN equations of motion (11). Given the initial condition of T at the reference time, Equation (28) gives us the pulse emission time t_e at the center-of-mass frame. However, in pulsar timing, it is used to redefine the pulsar's proper time and to absorb the linear dependence of t in T , which corresponds to a redefinition of the pulsar spin and its time derivative in the pulsar's proper frame (Blandford & Teukolsky 1976). Though the effects of the SMBH spin and quadrupole moment in the pulsar's orbital motion make it hard to strictly define a constant scaling factor for T that absorbs all the linear dependence, as there are several different precession time scales in the system, we can still use a leading-order approximation,

$$T \rightarrow f_E T \equiv \left(1 - \frac{2GM}{ac^2} - \frac{E}{c^2} \right) T, \quad (30)$$

where E is the orbital energy at the Newtonian order. These transformation fully degenerates with the redefinition of ν and $\dot{\nu}$, and thus will not affect the parameter estimation for parameters that we are interested in. After this redefinition, one can introduce the so-called Einstein delay that accounts for the rest difference between T and t (Blandford & Teukolsky 1976),

$$\Delta_E = t - T, \quad (31)$$

and we calculate it by integrating

$$\frac{d\Delta_E}{dt} = 1 - \frac{1}{f_E} \left[1 - \frac{GM}{rc^2} - \frac{1}{2} \frac{v^2}{c^2} + \frac{1}{2} \left(\frac{GM}{rc^2} \right)^2 - \frac{3}{2} \frac{GM}{rc^2} \frac{v^2}{c^2} - \frac{1}{8} \frac{v^4}{c^4} \right], \quad (32)$$

together with the equations of motion (11).

The emission time of the pulse in the global coordinate can then be expressed as

$$t_e = T_e + \Delta_E, \quad (33)$$

and taking into account the propagation time delay, the TOA of pulse is

$$t^{\text{TOA}} = t_e + \Delta_R + \Delta_{S1} + \Delta_{S2} + \Delta_{FD}. \quad (34)$$

Equations (21), (27), (33) and (34)—together with the equations of motion for the pulsar—compose the basic timing model for the pulsar-SMBH system.

Before we proceed, we discuss here the effects of the proper motion of Sgr A*. In previous discussions, we always assume that the distance between Sgr A* and SSB tends to infinity. However, the distance between Sgr A* and SSB is about $d = 8.2$ kpc (Abuter et al. 2020) and the proper motion of Sgr A* has been precisely measured by the Very Long Baseline Array (VLBA) observation (Reid & Brunthaler 2020). The apparent motion of Sgr A* is about -6.4 mas yr⁻¹ along the Galactic plane and -0.22 mas yr⁻¹ toward the North Galactic Pole, which can be mainly attributed to the Sun's orbital motion around the GC. This relative motion between Sgr A* and SSB causes several apparent effects in the timing observation which are discussed below.

The proper motion of the pulsar-SMBH system changes its geometrical orientation with respect to the Earth, including the secular changes in the orbital inclination angle i and the longitude of orbital periastron ω (Kopeikin 1996),

$$\delta i = (-\mu_\alpha \sin \Omega + \mu_\delta \cos \Omega)t, \quad (35a)$$

$$\delta \omega = \sin^{-1} i (\mu_\alpha \cos \Omega + \mu_\delta \sin \Omega)t, \quad (35b)$$

where μ_α and μ_δ are the components of the proper motion along $\hat{\mathbf{I}}_0$ and $\hat{\mathbf{J}}_0$ directions respectively. Note that the effects of proper motion depend on the longitude of the ascending node Ω , which is usually not an observable in the timing observation of systems with negligible proper motion. The proper motion breaks the rotation symmetry of the system in the timing observation and provides the possibility of measuring Ω . Taking the proper motion of Sgr A*, one can estimate that the apparent change rates of i and ω are at the order of

10^{-6} deg yr⁻¹, which corresponds to a cumulated time delay of ~ 10 ms for a pulsar in a 1-yr orbit and a total observation time span of 5 years. This suggests that in future observations, one has the possibility to measure the proper motion effects. In our timing model, we incorporate the proper motion by applying a coordinate rotation before we calculate the Römer delay Δ_R introduced in Section 2.1, i.e., we replace $\hat{\mathbf{K}}_0$ with

$$\hat{\mathbf{K}}_0 \rightarrow \hat{\mathbf{K}}_0 \cos \mu t + \left(\frac{\mu_\alpha}{\mu} \hat{\mathbf{I}}_0 + \frac{\mu_\delta}{\mu} \hat{\mathbf{J}}_0 \right) \sin \mu t, \quad (36)$$

in Equation (1), where $\mu = \sqrt{\mu_\alpha^2 + \mu_\delta^2}$. In principle, this rotation should be applied to the calculations of all other delays. However, the PN-proper motion crossing terms are clearly beneath the observation precision and thus they can be ignored.

The relative motion between Sgr A* and SSB may also introduce apparent change in the pulsar orbital period via $\dot{P}_b/P_b = \dot{D}/D$, where D is the Doppler shift of the system (Damour & Taylor 1992). However, considering that the motion of the Sun is largely described by a circular motion around the GC, the Shklovskii effect (Shklovskii 1970) and the Galactic gravitational acceleration effect will be canceled and thus can be ignored in the timing model.

As an illustration, in Figure 2 we plot the various time delays in the timing model for the system with parameters in Equation (17). To calculate the aberration delay and proper motion effects introduced in this subsection, we have further set the parameters of the pulsar, $\Theta_{\text{PSR}} = \{N_0, \nu, \dot{\nu}, \lambda_p, \eta_p\}$, to be

$$\begin{aligned} N_0 &= 0.5, & \nu &= 1 \text{ Hz}, & \dot{\nu} &= 10^{-15} \text{ s}^{-2}, \\ \lambda_p &= \pi/5, & \eta_p &= 0, \end{aligned} \quad (37)$$

where λ_p and η_p give the spin direction of the pulsar, and we set it to be in parallel with the orbital angular momentum in the fiducial case. We also add the proper motion μ_α and μ_δ to the SMBH parameter set Θ_{SMBH} and have used the values in Reid & Brunthaler (2020),

$$\mu_\alpha = -3.2 \text{ mas yr}^{-1}, \mu_\delta = -5.6 \text{ mas yr}^{-1}. \quad (38)$$

2.4. The inverse timing model

In previous subsections, we have built a timing model for pulsar-SMBH systems accurate to the 2PN level. The timing model predicts the TOA of a pulse emitted at a given pulsar proper time, for example, the time when pulsar's rotation number N is an integer. By fitting the predictions to the observed TOAs, one can obtain the best-fit parameters in the timing model. However, in the real pulsar timing process, the direct observable is the TOAs of the pulses. Due to the fact that telescopes will not observe a pulsar continuously to record

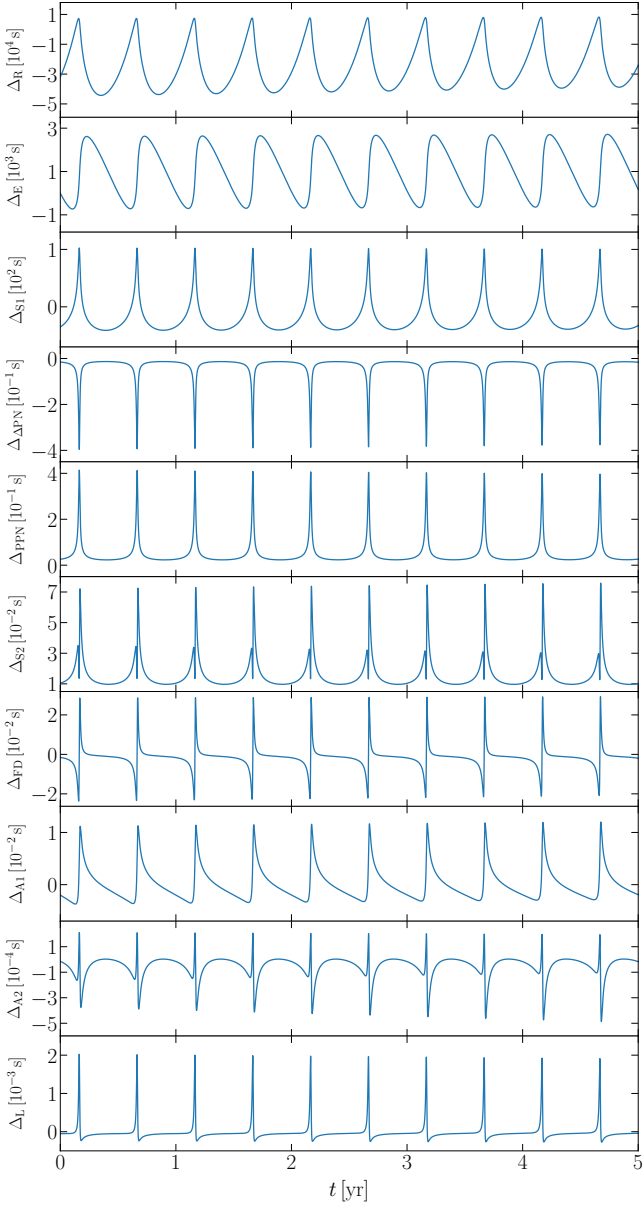


Figure 2. Various time delays described in the text for the fiducial pulsar-SMBH system. A constant term is removed from the 1PN Shapiro delay with respect to Equation (2).

every single pulse, we, in fact, do not know the pulsar rotation number N corresponding to the observed TOAs. Thus, the timing residual, which represents the difference between the model prediction and observation, is defined to be (Damour & Deruelle 1986)

$$\mathcal{R} = \frac{1}{\nu} \left[\mathcal{N}(t^{\text{TOA}}; \{\Theta\}) - \lfloor \mathcal{N}(t^{\text{TOA}}; \{\Theta\}) \rfloor \right], \quad (39)$$

where $\mathcal{N}(t^{\text{TOA}}; \{\Theta\})$ is the predicted pulsar's rotation number for the pulse arrived at t^{TOA} and with model parameters $\{\Theta\}$; note that it needs not to be an integer.

$\lfloor \mathcal{N}(t^{\text{TOA}}; \{\Theta\}) \rfloor$ is the integer closest to $\mathcal{N}(t^{\text{TOA}}; \{\Theta\})$. This definition folds the timing residual into one pulsar's rotation period, and thus it is necessary to have a timing model accurate than the pulsar's rotation period. Equation (39) requires the calculation of pulsar rotation number from a given TOA, and the function $\mathcal{N}(t^{\text{TOA}}; \{\Theta\})$ is realized by the so-called inverse timing model (Damour & Deruelle 1986). For analytical timing models that adopt a PN expansion, the inverse timing model can be obtained by solving Equations (27), (33), and (34) with iteration (Damour & Deruelle 1986). However, to invert the numerical timing model, in general, one may need to calculate a series of TOAs corresponding to different N and invert the numerical relation by interpolation (Della Monica & de Martino 2025). The choice of the sample rate of the numerical relation and the interpolation procedure may introduce additional numerical errors to the inverse timing model. Besides, a higher sample rate generally needs more computational resources, which may not be always available in parameter estimation with, say, Monte Carlo techniques, which needs many calculations of the inverse timing model with different model parameters.

Hu et al. (2023) proposed a method for building the inverse timing model efficiently. Instead of integrating Equation (11), one can transform the integration variable from coordinate time t to t^{TOA} by taking the advantage that Equation (34) has an analytical expression that only depends on the pulsar's position at time t .² Writing out explicitly, one has

$$\frac{dt^{\text{TOA}}}{dt} = 1 + \frac{d\Delta_{\text{R}}}{dt} + \frac{d\Delta_{\text{S}}}{dt} + \frac{d\Delta_{\text{FD}}}{dt}, \quad (40)$$

where

$$\begin{aligned} \frac{d\Delta_{\text{R}}}{dt} = \frac{1}{c} & \left[v_z \cos \mu t + \left(\frac{\mu_\alpha}{\mu} v_x + \frac{\mu_\delta}{\mu} v_y \right) \sin \mu t \right] \\ & + \frac{1}{c} \left[(\mu_\alpha x + \mu_\delta y) \cos \mu t - \mu z \sin \mu t \right], \end{aligned} \quad (41a)$$

$$\frac{d\Delta_{\text{S}}}{dt} = \frac{d\Delta_{\text{S1}}}{dt} + \frac{d\Delta_{\Delta\text{PN}}}{dt} + \frac{d\Delta_{\text{PPN}}}{dt}, \quad (41b)$$

$$\frac{d\Delta_{\text{S1}}}{dt} = -\frac{2GM}{c^3} \frac{\dot{r} - v_z}{r - z}, \quad (41c)$$

$$\frac{d\Delta_{\Delta\text{PN}}}{dt} = \frac{4G^2 M^2}{c^5} \frac{\dot{r} - v_z}{(r - z)^2}, \quad (41d)$$

$$\begin{aligned} \frac{d\Delta_{\text{PPN}}}{dt} = \frac{G^2 M^2}{4c^5} & \left[-\frac{v_z}{r^2} + \frac{2z\dot{r}}{r^3} + 15 \frac{v_z - \dot{r}z/r}{r^2 - z^2} \right. \\ & \left. - 15 \arccos\left(-\frac{z}{r}\right) \frac{r\dot{r} - zv_z}{(r^2 - z^2)^{3/2}} \right], \end{aligned} \quad (41e)$$

² Here we omit the lower index e and take this equation as a general relation between coordinate time t and arrival time t^{TOA} .

$$\frac{d\Delta_{\text{FD}}}{dt} = -\chi \frac{2G^2 M^2}{c^5} \left\{ \frac{\hat{\mathbf{s}} \cdot \left[\hat{\mathbf{K}}_0 \times (\mathbf{v}/r - \hat{\mathbf{n}}\dot{r}/r) \right]}{r-z} - \frac{\hat{\mathbf{s}} \cdot \left(\hat{\mathbf{K}}_0 \times \hat{\mathbf{n}} \right) \dot{r} - v_z}{r-z} \right\}, \quad (41f)$$

with (x, y, z) and (v_x, v_y, v_z) the coordinate components of pulsar position and velocity, respectively. In the Römer delay, we have taken into account the proper motion of Sgr A* as discussed before.

Using Equation (40), one may integrate the following system

$$\frac{d}{dt^{\text{TOA}}} \begin{pmatrix} \mathbf{r} \\ \mathbf{v} \\ t \\ \Delta_E \end{pmatrix} = \begin{pmatrix} \mathbf{v} \\ \ddot{\mathbf{r}} \\ 1 \\ d\Delta_E/dt \end{pmatrix} \frac{dt}{dt^{\text{TOA}}}(\mathbf{r}, \mathbf{v}, t), \quad (42)$$

with $\ddot{\mathbf{r}}$ and $d\Delta_E/dt$ given by Equations (11) and (32), respectively. The initial condition for the above differential system can also be transformed from the original initial condition. Here, we take the reference time to be $t^{\text{TOA}} = 0$ when the pulsar has initial position \mathbf{r}_0 and velocity \mathbf{v}_0 given by its orbital elements. One can calculate the corresponding coordinate time t with the equations of various time delays. Finally, we choose $\Delta_E = 0$ at the reference time.

Integrating the system (42) then gives the system directly as functions of t^{TOA} . Given a TOA, one can read out the associated pulse emission time t and Einstein delay Δ_E directly from the integration output. One can then calculate T_e , T , and N using Equations (33), (27), and (21) sequentially. This method fully utilize the advantage of the adaptive integration method, as in general the TOA observation cadence is much longer than the integration time step that is needed for the desired integration precision.

In Appendix B, we give a more detailed discussion of the numerical accuracy of our code.

3. PARAMETER ESTIMATION

Based on the realistic timing model constructed in the previous section, we are able to forecast the future timing observation of possible pulsar-SMBH systems. In this section, we discuss the measurability of various system parameters using the Fisher matrix method. Some of these results were obtained in previous studies (Liu et al. 2012; Psaltis et al. 2016; Hu et al. 2023) based on timing models that only take into account some of the previously discussed effects. Those earlier results remain valid when higher-order terms do not bother the parameter estimation dramatically. Nevertheless, we still

present more realistic results here as a verification and for completeness. Further, we discuss the effects related to the aberration and proper motion, which are considered for the first time in pulsar-SMBH systems. This section is constructed as follows. In Section 3.1, we introduce the parameter estimation method and numerical setup for our analysis. In Section 3.2, we forecast the measurability of the parameters of the GC SMBH, Sgr A*. We discuss the effect of the proper motion of Sgr A* in Section 3.3. The detectability of the pulsar's spin direction based on aberration effects is discussed in Section 3.4.

3.1. The Fisher matrix method

As we introduced before, the timing residual (39) for a pulse arrived at t^{TOA} can be calculated with the inverse timing model after giving all the system parameters Θ ,

$$\Theta = \Theta_{\text{SMBH}} \cup \Theta_{\text{orb}} \cup \Theta_{\text{PSR}}, \quad (43)$$

where

$$\Theta_{\text{SMBH}} = \{M, \chi, \lambda, \eta, q, \mu_\alpha, \mu_\beta\}, \quad (44a)$$

$$\Theta_{\text{orb}} = \{P_b, e, i, \omega, \Omega, T_0\}, \quad (44b)$$

$$\Theta_{\text{PSR}} = \{N_0, \nu, \dot{\nu}, \lambda_p, \eta_p\}. \quad (44c)$$

However, for separating out the rotation symmetry, we in fact use $\eta - \Omega$ and $\eta_p - \Omega$ instead of η and η_p . As we will discuss later, even with known proper motion, the measurement precision of Ω is not high.

Assuming a Gaussian timing noise in the observation, the probability for the system to have parameters Θ is

$$P(\Theta|\{t^{\text{TOA}}\}) \propto \exp\left(-\frac{1}{2} \sum_{i=1}^{N_{\text{TOA}}} \frac{\mathcal{R}(t_i^{\text{TOA}}; \Theta)^2}{\sigma_{\text{TOA},i}^2}\right), \quad (45)$$

where the expression for \mathcal{R} is given in Equation (39) and the summation is over all observed TOAs denoted by $\{t^{\text{TOA}}\}$. $\sigma_{\text{TOA},i}$ is the timing precision for the i -th TOA. As discussed before, due to the fact that we cannot know the true value of the pulsar's rotation number related to an observed pulse, in the right-hand side of Equation (39), the second term is chosen to be the closest integer to the first term. However, in the Fisher matrix analysis of simulated data sets, it will be convenient to use $N(t^{\text{TOA}}; \Theta)$ instead of the second term, where $\bar{\Theta}$ represents the true value of the system parameters that are used in simulations. This replacement will be valid if the timing noise and model inaccuracy are smaller than the pulsar's rotation period.

As a standard procedure, the covariance matrix in the Fisher formalism, defined by

$$C_{\alpha\beta} = \left(\frac{\partial^2 \mathcal{L}}{\partial \Theta^\alpha \partial \Theta^\beta} \right)^{-1}, \quad (46)$$

can serve to obtain an estimation of the measurement uncertainties of the parameters, where $\mathcal{L} = -\ln P(\Theta|\{t^{\text{TOA}}\})$ is the log-likelihood function. For the purpose of estimation, and considering the replacement discussed before, Equation (46) can be well approximated by

$$C_{\alpha\beta} = \left(\frac{1}{\nu^2} \sum_{i=1}^{N_{\text{TOA}}} \frac{1}{\sigma_{\text{TOA},i}^2} \frac{\partial \mathcal{N}_i}{\partial \Theta^\alpha} \frac{\partial \mathcal{N}_i}{\partial \Theta^\beta} \right)^{-1}, \quad (47)$$

where $\mathcal{N}_i = \mathcal{N}(t_i^{\text{TOA}}; \Theta)$, and the above equation is evaluated at $\bar{\Theta}$. Equation (47) is equivalent to Equation (46) if no noise is present, and it only requires the evaluation of the first-order derivative of the inverse timing model. We shall note that the numerical differentiation performed here needs additional care, and more numerical details are discussed in Appendix C.

Finally, we shall notice that, though we list all the system parameters in Equation (44), for timing-only observations and distant pulsars, there always exists a rotation symmetry around the line of sight. In principle, one needs fix at least one parameter among Ω , η , μ_α , μ_δ , and η_p . Considering that η_p is only related to the aberration effect, and η in general is considered together with the other two spin parameters, in the later discussion, we group Ω and the proper motion parameters, and will always fix Ω , or μ_α and μ_δ .

3.2. Measurability of SMBH parameters

Now we forecast the measurability of the SMBH mass, spin, and quadrupole moment based on mock data simulations. As we will discuss later, here we choose to treat the proper motion of SMBH as known parameters, i.e., we fix μ_α and μ_δ for parameter estimation here. Though we have considered higher-order effects in our timing model, the measurement precision of SMBH mass, spin, and quadrupole moment should not show significant differences from previous studies that used a timing model with only some leading-order effects (Liu et al. 2012; Psaltis et al. 2016; Hu et al. 2023). This can serve as a check for our numerical procedure. In reality, when the effects from higher-order terms are larger than the timing precision, our timing model should be used.

We simulate a system with system parameters given in Equations (17), (37), and (38), for weekly observations spanning 5 years, which in total give 260 TOAs. The timing precision of a normal pulsar in the GC region for future SKA-like telescopes may reach 1 ms or even better (Liu et al. 2012), thus we assume that the timing precision $\sigma_{\text{TOA}} = 1$ ms for all TOAs. Other precision can be easily rescaled from our results.

In Figure 3 (a), we show the fractional precision of the SMBH parameters as functions of the pulsar orbital

period. As expected in previous studies (Liu et al. 2012; Psaltis et al. 2016; Hu et al. 2023), for pulsars with orbital periods $P_b \lesssim 0.5$ yr, the measurement precision of SMBH mass, spin, and quadrupole moment can all be better than 1% level, which can provide a stringent test of the no-hair theorem.

One may notice that there are lots of spike structures in the curves shown in Figure 3 (a). As verified in Appendix C, we reckon that these structures are at least real results for the Fisher matrix approximation instead of being caused by numerical errors. In this figure, for each curve we plot 5000 points so that one can see detailed structures. These spikes are centered around positions where P_b is an integer (rational) multiple of weeks. As in the parameter estimation, we assumed an observational cadence of exactly one week. In real observations, one will not expect the pulsar-SMBH system to locate in such a peak, and the observational cadence will also be more complex and relatively irregular, which will smooth these structures. In contrast, the step-like structure around $P_b \sim 2.5$ yr is due to an additional periastron passage being observed, which will also occur for real observations where the total time spans only cover one or two orbits.

Figure 3 (b) shows the fractional precision of the SMBH parameters as functions of the orbital eccentricity, while the pulsar orbital period is fixed to $P_b = 0.5$ yr. Same as before, each curve here contains 5000 points. As we discussed in Hu et al. (2023), the fractional precision depends on $1 - e^2$ in a nearly power-law manner. All the results shown here are consistent with previous studies.

3.3. The effects of proper motion

In previous figures, we showed the results that all parameters in Equation (44), except the proper motion parameters μ_α and μ_δ , are treated as free parameters. The proper motion of Sgr A* breaks the rotation symmetry around the line of sight and specifies a sky orientation, enabling a measurement of the longitude of the ascending node Ω . Previous studies suggested that a measurement of Ω may help us break the leading-order degeneracy in the measurement of spin components (Zhang & Saha 2017; Hu et al. 2023). Therefore we study the effects of the proper motion here.

We first study the measurement precision of Ω , or the proper motion parameters μ_α and μ_δ , when only timing data are considered. As mentioned before, the VLBA observations have measured the proper motion of Sgr A* to a relatively high precision (Reid & Brunthaler 2020), therefore μ_α and μ_δ can be treated as fixed parameters in timing data analysis. Nevertheless, one can also fix Ω to obtain a timing-only measurement of the proper mo-

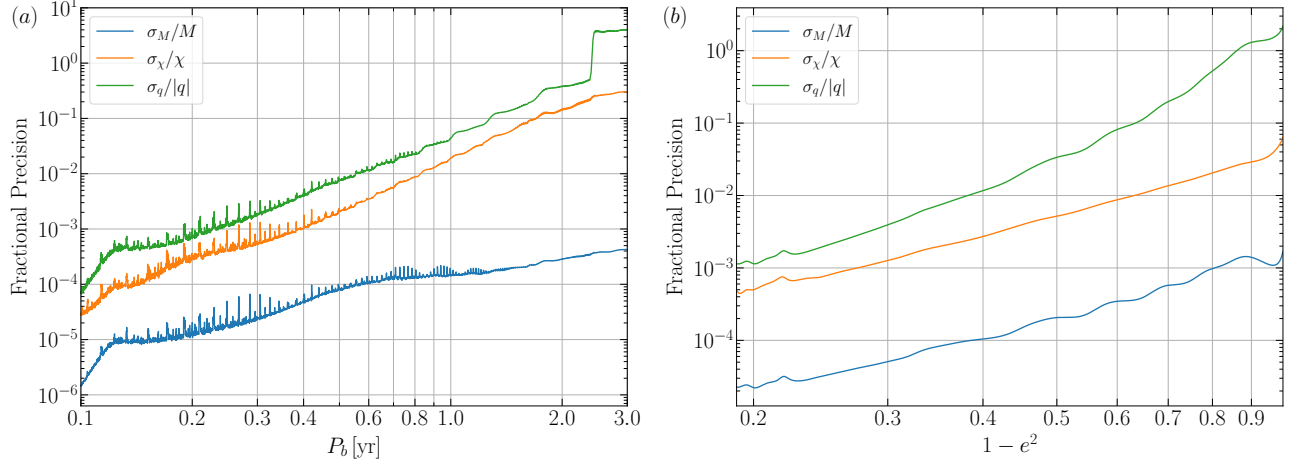


Figure 3. The fractional precision of SMBH parameters as functions of the pulsar’s (a) orbital period and (b) orbital eccentricity.

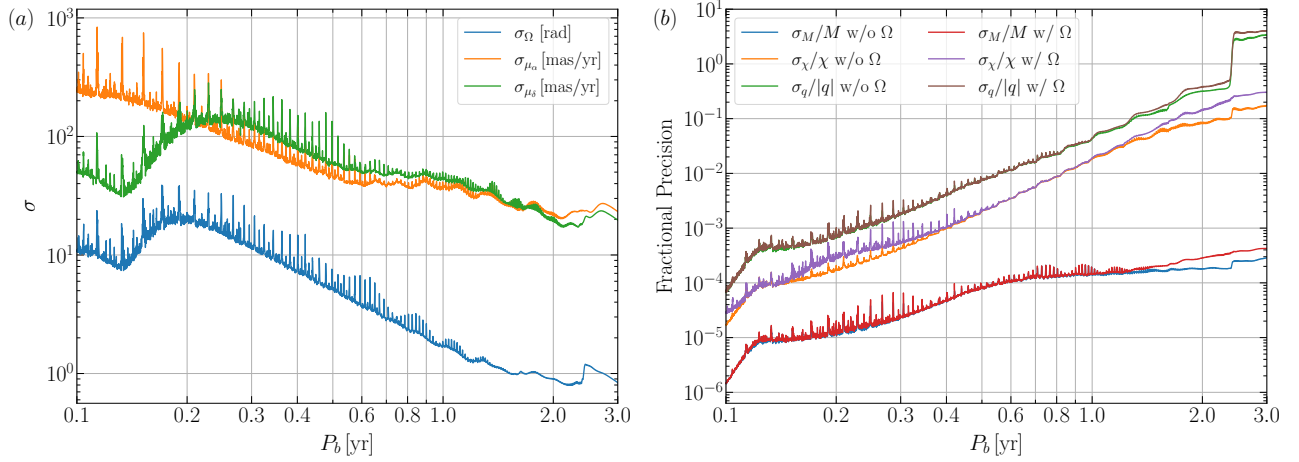


Figure 4. (a) The measurement precision of the proper motion parameters μ_α and μ_δ , and the longitude of the ascending node Ω . Due to the degeneracy caused by the rotation symmetry, for estimating the measurability of the proper motion parameters, we fix Ω , and vice versa, we fix the proper motion parameters when estimating the measurement precision of Ω . (b) Comparison of parameter estimation results with or without considering the proper-motion effect. For parameter estimation that does not consider the proper motion, we fix $\Omega = 0$ without losing generality.

tion; in this case, the direction of the proper motion is referenced to the pulsar’s orbit. In principle, only when the timing-only measurement precision is much worse than the VLBA measurement precision, the previously adopted treatment is valid. In Figure 4 (a), we show the expected measurement precision of the proper motion parameters and the longitude of the ascending node from timing observation. Due to the degeneracy caused by the rotation symmetry, when estimating the proper motion parameters, we fix the longitude of the ascending node, and vice versa. One can see that the expected measurement precisions of the proper motion parameters μ_α and μ_δ are worse than 10 mas/yr from timing-only observation, which is far worse than the VLBA ob-

servations. Therefore, it is better to fix the value of the proper motion parameters to the VLBA measurement, which accounts for the proper-motion effect with enough accuracy.

Fixing the proper motion parameters then enables a measurement of the longitude of ascending node Ω of the pulsar’s orbit, as the proper motion breaks the rotation symmetry (Kopeikin 1996). However, from the figure we can see that, for pulsars with small orbits, one can still hardly determine the value of Ω .³ For pulsars with larger orbits, the measurement precision in Ω be-

³ Note that the unit of σ_Ω in the figure is radian.

comes better. As discussed in Section 2.3, the effects of the proper motion are effectively reflected in the Römer delay, which is proportional to the orbital length scale, while the precession rate caused by proper motion effects is fixed.

Previous studies have pointed out that there is a leading-order degeneracy among the spin parameters, $\{\chi, \lambda, \eta\}$, of the SMBH. This degeneracy largely limits the measurement precision of the SMBH spin (Liu et al. 2012; Zhang & Saha 2017; Hu et al. 2023; Hu & Shao 2024). The leading-order degeneracy also originates from the rotation symmetry in the pulsar timing technique. Roughly speaking, the spin-orbit coupling causes additional precession in i , ω , and Ω . However, for timing observation in a short time span, only \dot{i} and $\dot{\omega}$ are observable, which cannot fully determine the three spin parameters (Liu et al. 2012). Therefore, to break this degeneracy, one possibility argued in previous studies is to combine the proper motion information (Zhang & Saha 2017), which enables a measurement of $\dot{\Omega}$. However, from Figure 4 (a) one can see that, even with known proper motion parameters, for pulsars with short orbital periods, the measurement precision of Ω is quite low (e.g., for $P_b \lesssim 1$ yr, one has $\sigma_\Omega \gtrsim 2$ rad). This low precision suggests that for pulsars with small orbital periods, introducing the proper-motion effect cannot break the leading-order degeneracy efficiently. For pulsars with much larger orbital periods, as studied by Zhang & Saha (2017), combining the astrometric observation might help. In real observations, one may also break this leading-order degeneracy by combining the timing observation of two or more pulsars if they are observed (Hu & Shao 2024).

In Figure 4 (b), we give a comparison of the parameter estimation results with and without considering the proper-motion effects and parameter Ω . In previous studies, without considering the proper motion of Sgr A*, Ω is not measurable, so that it is excluded from parameter estimation. However, for real observations, the proper motion of Sgr A* can be non-negligible, especially for pulsars with large orbital periods. Therefore, including parameter Ω in parameter estimation might be necessary. From the figure, one can see that the proper motion only introduces a small difference in the measurement precision of SMBH parameters, as it is a small effect. Also, as expected, the influence is generally larger for pulsars with large orbital periods. Nevertheless, in this work, we treat Ω as a free parameter that needs to be estimated.

3.4. The aberration effects

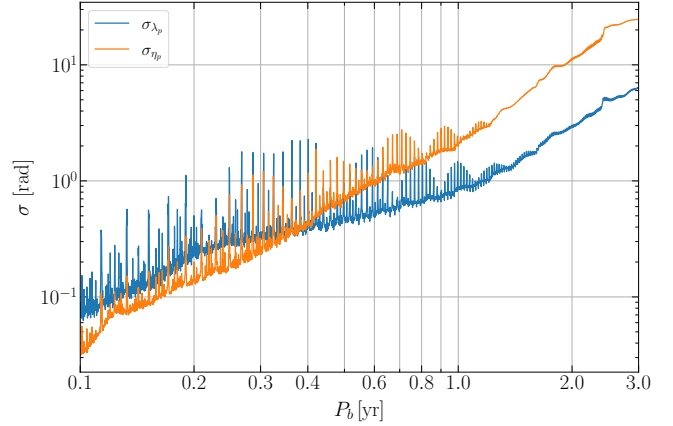


Figure 5. Expected measurement precision of λ_p and η_p as functions of the pulsar orbital period P_b .

In Section 2.3, we discussed the aberration delays, including Δ_{A1} , Δ_{A2} and Δ_L , which come from the rotation origin of the pulsar’s “lighthouse” pulse. Though discussed in Damour & Deruelle (1986), the leading-order aberration effect will be absorbed in a redefinition of various timing parameters, we have to include them here for the following reasons. First, different from the DD timing model constructed by Damour & Deruelle (1986), which parameterized the various effects in a theory-independent way, the timing model discussed in this paper is directly based on the physical parameters. Each of the parameters might account for several effects both in the pulsar orbital motion and light propagation. Therefore, the aberration effect might not be able to be fully absorbed by other parameters in our pulsar-SMBH timing model. Further, as shown in the previous section, the amplitude of the aberration delay can be as large as 10 ms, which is larger than the expected timing precision. As argued by Damour & Deruelle (1986) and Kramer et al. (2021), the aberration delay needs to be considered in order to give an unbiased parameter estimation result.

However, different from other effects, all three aberration effects include the additional parameters λ_p and η_p that describe the direction of the pulsar spin axis \hat{e}_3 . As discussed in Section 2.2, the precession time scale of the pulsar spin axis is much longer than the corresponding time scale in usual comparable-mass binary pulsar systems. Therefore, it might be hard to obtain the geometry of the pulsar using pulse-profile analysis (Ferdman et al. 2013). The direction of the pulsar spin axis then needs to be determined from the timing observation.

In Figure 5, we plot the expected measurement precision of the parameters λ_p and η_p as functions of the pulsar’s orbital period. As the aberration effects are

suppressed by the factor of P/P_b , where P is the rotation period of the pulsar, for larger orbital periods, the constraints on λ_p and η_p are weaker. For pulsars with orbital periods $P_b \lesssim 1$ yr, one might measure the directional angle of the pulsar spin axis to a precision around or better than 1 rad through timing-only observations for a reasonable observation time span.

4. PRESENCE OF TIMING RED NOISE

The parameter estimation in the previous sections was based on the probability function given in Equation (45), where we assumed a Gaussian noise realization. However, it is well known that for pulsar timing, there can exist a red noise component in the timing residual due to various reasons (Hobbs et al. 2010). Apart from the main contribution that comes from the rotation irregularity of the pulsar itself, for pulsars in the GC region, the dispersion measure variation and strong scattering of the interstellar medium may also introduce additional red noise.

The procedures of timing analysis in the presence of red noise have long been developed (Coles et al. 2011; Lentati et al. 2013; Parthasarathy et al. 2019), as it is important for studying the pulsar physics (Greenstein 1970; Lyne et al. 2010) as well as understanding their sensitivity to nHz-frequency gravitational waves (Caballero et al. 2016; Lentati et al. 2016; Lam et al. 2017; Agazie et al. 2023). In the context of testing gravity theories using binary pulsars, the red noise is often ignored, as the best results usually come from millisecond pulsars (Kramer et al. 2021), which have much smaller intrinsic red noise compared to normal pulsars. Further, the tight orbit of a binary pulsar usually required by testing relativistic gravity also makes a clear separation between the interested time scale—in most cases, the orbital time scale—and the red noise time scale, say, the observation time span, so that the red noise effects on the interested parameters are negligible in many situations (Kramer et al. 2021).

However, for a pulsar orbiting around Sgr A* considered in this paper, it might be worthwhile to study the red noise effects in timing analysis. As mentioned above, for pulsars in the GC region, there might be red noise contributions from the complex environment. Further, it is expected that we are more likely to find normal pulsars in that region from an observational point of view, because the interstellar scattering may prevent identifying the pulses of millisecond pulsars (Schoedel et al. 2024). Therefore, if we find a normal pulsar, a large intrinsic timing red noise of the pulsar may exist. A pulsar-SMBH system is also different from the usual binary pulsar systems in its orbital time scale, which can

be on the order of years. For a 5-yr observation time span considered in this paper, the red noise time scale is not clearly separated from the orbital time scale, thus it might cause larger effects to the parameter estimation results.

Considering the above motivations, in this section, we study the red noise effects in the parameter estimation. In Section 4.1, we describe our red noise model. The design matrix approximation is introduced in Section 4.2. We present a modified Fisher matrix analysis with the assumption that we know the red noise parameters in Section 4.3. We show results of Bayesian analysis that estimate the system parameters and red noise parameters simultaneously in Section 4.4.

4.1. Red noise model

The red noise component in the timing noise power spectrum density can be simply described by a (two-sided) power-law spectrum,

$$P_{\text{red}}(f) = \frac{A_r^2}{12\pi^2} \left(\frac{f}{f_{\text{yr}}} \right)^{-\alpha}, \quad (48)$$

where A_r is the red noise amplitude in the unit of $\text{yr}^{3/2}$, α is the spectrum index, and $f_{\text{yr}} = 1 \text{ yr}^{-1}$. However, for simulating a finite noise realization and for the convenience in the later analytical analysis without the need to deal with various divergence terms, we adopt a cut-off power law spectrum (Coles et al. 2011)

$$P_{\text{red}}(f) = \frac{A}{[1 + (f/f_c)^2]^{\alpha/2}}, \quad (49)$$

where f_c is a cut-off frequency for the low-frequency part, and

$$A = \frac{A_r^2}{12\pi^2} \left(\frac{f_c}{f_{\text{yr}}} \right)^{-\alpha}. \quad (50)$$

Due to the fact that one always fits the pulsar's rotation, characterized by N_0 , ν and $\dot{\nu}$, in the timing model, the spectrum will always be flattened below the frequency $1/T_{\text{obs}}$. For $f_c < 1/T_{\text{obs}}$, the cut-off power-law spectrum is equivalent to the simple power law for our purpose. Therefore, we fix $f_c = 1/50 \text{ yr}^{-1}$ in this paper. We have verified that changing f_c does not affect our results significantly.

Figure 6 (a) shows two noise realizations, including both red noise and white noise, but with different red noise amplitudes. For the white-noise component, we consider $\sigma_{\text{TOA}} = 1$ ms as used in previous sections, and the realizations are shown by the blue-dotted line. We also show the post-fit residuals of the noise realizations. In the figure f_2 denotes the timing residuals after a

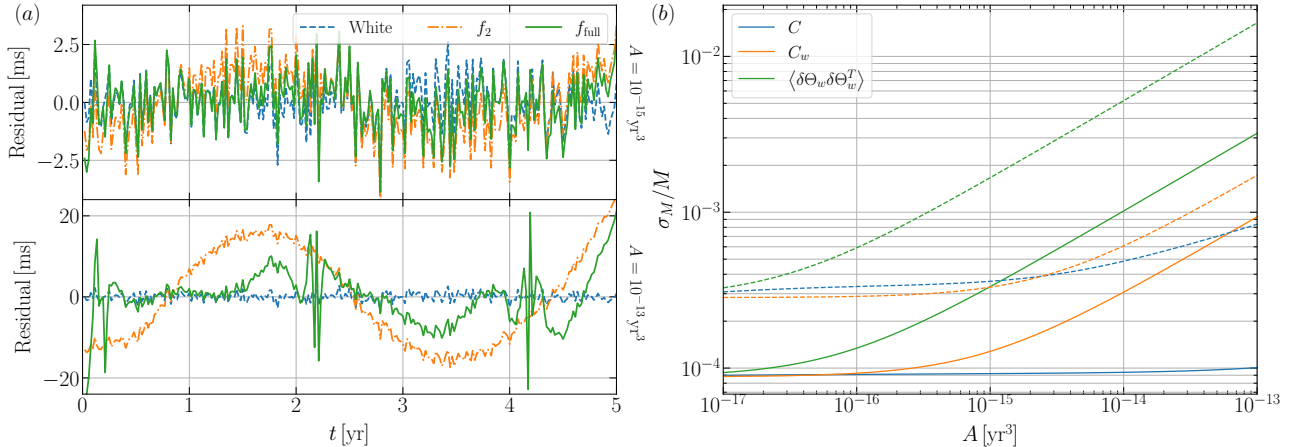


Figure 6. (a) Two noise realizations with different red noise amplitude A . The power-law index is chosen to be $\alpha = 5$ for both panels. The white-noise components are shown by the blue dashed line and we have used $\sigma_{\text{TOA}} = 1$ ms. f_2 denotes the timing residuals after a second-order polynomial fitting that subtracts the pulsar rotation’s contribution via N_0 , ν , and $\dot{\nu}$. f_{full} denotes the timing residuals after a fitting of the linearized full timing model. Note that the fitting here is a simple least-square fitting which does not consider noise properties. (b) The fractional precision of the mass of SMBH as a function of the red noise amplitude estimated by three different methods shown in Equations (61), (65), and (68). For the covariance matrix C_w we use the noise averaged $\sigma_{w,\text{eff}}^2$ shown in Equation (66). The solid line shows the results for a pulsar-SMBH system with system parameters same as in Section 2, while the dashed line shows a similar system but with a larger orbital period $P_b = 2$ yr.

second-order polynomial fitting that subtracts the pulsar’s rotation contribution (via parameters N_0 , ν , and $\dot{\nu}$); f_{full} denotes the timing residual after a fitting of the linearized full timing model that is introduced later in this subsection. For the linearized full timing model, the system parameters are described in Section 2 except that here we use $P_b = 2$ yr. The clear absorption of the timing residuals by the linearized full timing model suggests the existence of strong biases in system parameters besides N_0 , ν , and $\dot{\nu}$.

The amplitude A and power-law index α can vary a lot for different pulsars. Here we choose the values of A and α motivated by the studies of a large sample of pulsars (Shannon & Cordes 2010; Parthasarathy et al. 2019). For normal pulsars, the spectrum index α peaks around 5, and the red noise amplitude varies around $A_r \sim 10^{-10} \text{ yr}^{-3/2}$ for more than one dex. Transforming this value to A as a reference, in Figure 6, we choose $A = 10^{-15} \text{ yr}^3$ to represent a case where the red noise is relatively weak and comparable to the white noise, and a case where $A = 10^{-13} \text{ yr}^3$ which represents a situation where the pulsar has a strong red noise dominating.

In this work, we ignore the red noise contribution caused by the dispersion measure variation. Though, as mentioned before, the complex astrophysical environment in the GC region may introduce a relatively large red noise contribution, they can be treated similarly to the pulsar’s intrinsic red noise in real data analysis. Including it will only introduce another power-law component in the noise spectrum (Chen et al. 2025). Further,

the contribution from dispersion measure variation has an additional dependence on the observation frequency as $P_{\text{DM}} \propto \nu_{\text{obs}}^{-4}$, which might be reduced using higher-frequency and multi-frequency observations.

4.2. Design matrix approximation

Discussions in Section 3 used noiseless simulated data sets for prospecting the measurement precision of various system parameters. In the presence of noise, in principle, one shall use the fully non-linear timing model constructed in Section 2 to fit the TOAs and find the best-fit parameters. In this investigation, as we are only aiming to study the possible effects caused by the presence of red noise, we adopt the simplification of the design matrix. That is, one may expand the non-linear timing model around a system parameter set that is close enough to the best-fit point, and only takes the linear order of the timing model that is described by the design matrix,

$$\mathcal{M}_{i\mu} = -\frac{1}{\nu} \frac{\partial \mathcal{N}_i}{\partial \Theta^\mu}. \quad (51)$$

For real observations, the expansion point can be obtained by, for example, a primary fit. Here we simply expand the timing model around the system’s true parameter set $\bar{\Theta}$, which is valid as long as the noise is small. This choice is also equivalent to the Fisher matrix approximation in the case of pure white noise, as the covariance matrix in the Fisher matrix approxima-

tion defined by Equation (47) has the form

$$C_{\alpha\beta} = \left(\sum_i \frac{1}{\sigma_{\text{TOA},i}^2} \mathcal{M}_{i\alpha} \mathcal{M}_{i\beta} \right)^{-1}. \quad (52)$$

With the above assumptions, the timing residuals in the presence of noise are

$$\begin{aligned} \mathcal{R}_i &= \frac{1}{\nu} \left[\mathcal{N}(t_i^{\text{TOA}}; \Theta) - \mathcal{N}(t_i^{\text{TOA}}; \bar{\Theta}) \right], \\ &= -\mathcal{M}_{i\mu} \delta\Theta^\mu + \delta t_i, \end{aligned} \quad (53)$$

where $\delta\Theta^\mu = \Theta^\mu - \bar{\Theta}^\mu$ as we expand the timing model around the system's true parameter set $\bar{\Theta}$. In Equation (53) a summation on μ is performed according to the Einstein summation convention. δt_i represents the pre-fit timing residuals⁴ and can be simulated by the noise model we discussed before. For the noiseless case, $\delta t_i = 0$, and it is clear that the best-fit parameters are the system's true parameters, as we do not consider mis-modeling effects here. However, in the presence of noise, maximizing a probability like Equation (45) will lead to a non-zero $\delta\Theta^\mu$ which depends on the noise realization.

4.3. Bias on parameter estimation

In the presence of red noise, the probability function is no longer described by Equation (45). Instead, we have

$$P(\Theta|t^{\text{TOA}}) \propto \exp\left(-\frac{1}{2} \mathcal{R}^T \mathcal{C}^{-1} \mathcal{R}\right). \quad (54)$$

Here and in the following, we use the matrix notation so that \mathcal{R} is the column vector constructed by N_{TOA} timing residuals, and \mathcal{C} is the $N_{\text{TOA}} \times N_{\text{TOA}}$ noise covariance matrix defined by

$$\mathcal{C} = \mathcal{C}_w + \mathcal{C}_r. \quad (55)$$

For the white noise contribution, we simply consider the form

$$\mathcal{C}_{w,ij} = \sigma_{\text{TOA}}^2 \delta_{ij}, \quad (56)$$

with δ_{ij} the Kronecker delta symbol, though for real observations and analysis it can be more complex (Chen et al. 2025). The red noise contribution is, by definition, the inverse Fourier transformation of the power spectral density, which reads

$$\mathcal{C}_{r,ij} = \langle \delta t_i \delta t_j \rangle = \int_{-\infty}^{\infty} P_{\text{red}}(|f|) e^{i2\pi f \tau_{ij}} df, \quad (57)$$

where $\langle \cdot \rangle$ is the average over noise realizations, and $\tau_{ij} = t_i^{\text{TOA}} - t_j^{\text{TOA}}$. Note that here we use the convention that

⁴ It is in fact the timing residuals after the primary fit, which gives $\bar{\Theta}$ in our assumption.

$P_{\text{red}}(f)$ is the two-sided power spectrum. For $P_{\text{red}}(f)$ in Equation (49), this is

$$\mathcal{C}_{r,ij} = \frac{2\pi^{\alpha/2} A}{\Gamma(\alpha/2)} f_c^{\frac{\alpha+1}{2}} |\tau_{ij}|^{\frac{\alpha-1}{2}} K_{\frac{\alpha-1}{2}}(2\pi f_c |\tau_{ij}|), \quad (58)$$

where $K_n(z)$ is the modified Bessel function of the second kind and $\Gamma(z)$ is the Gamma function. For $i = j$ one has

$$\mathcal{C}_{r,ii} = \pi^{1/2} A f_c \frac{\Gamma((\alpha-1)/2)}{\Gamma(\alpha/2)}. \quad (59)$$

If one knows exactly the power spectrum of the red noise and white noise, therefore the noise covariance matrix \mathcal{C} , one can simply maximize the probability function in Equation (54) within the linearized timing model and Equation (53) via (Coles et al. 2011)

$$\delta\Theta = (\mathcal{M}^T \mathcal{C}^{-1} \mathcal{M})^{-1} \mathcal{M}^T \mathcal{C}^{-1} \delta t, \quad (60)$$

for a given noise realization δt . The parameter estimation uncertainties and correlations are given by the covariance matrix

$$C = (\mathcal{M}^T \mathcal{C}^{-1} \mathcal{M})^{-1}. \quad (61)$$

However, in real observations, the noise parameters are *a priori* unknown. Estimation of the noise parameters with methods like the generalized least-square approach (Coles et al. 2011) or Bayesian approach (Chen et al. 2025) is needed and will be discussed in the next subsection. In the rest of this subsection, we aim to make an intuitive estimation of the biases caused by ignoring the red noise effects under the assumed red noise model, which highlights the importance of performing detailed noise analysis in pulsar-SMBH systems.

Using the probability function defined in Equation (45) assumes white noise that has the same strength for all TOAs. If the assumption holds, the post-fit residuals will have a χ^2 distribution with $N_{\text{TOA}} - N_{\text{param}}$ degrees of freedom, where N_{param} is the number of parameters that were used in the fitting. Therefore, from observational data, one may estimate the strength of the white noise via

$$\sigma_{w,\text{eff}}^2 = \frac{\mathcal{R}_w^T \mathcal{R}_w}{N_{\text{TOA}} - N_{\text{param}}}, \quad (62)$$

where $\sigma_{w,\text{eff}}$ is the effective timing precision estimated from data assuming purely white noise, and

$$\mathcal{R}_w = \delta t - \mathcal{M} (\mathcal{M}^T \mathcal{M})^{-1} \mathcal{M}^T \delta t, \quad (63)$$

is the post-fit timing residual.

In the presence of red noise, one may still use the above estimation, which will account for the red noise

by an effective white noise $\sigma_{w,\text{eff}}$. The best-fit parameter in this estimation is unbiased in the sense that

$$\langle \delta\Theta_w \rangle = (\mathcal{M}^T \mathcal{M})^{-1} \mathcal{M}^T \langle \delta t \rangle = 0, \quad (64)$$

where we use $\delta\Theta_w$ to distinguish it from the correct estimation $\delta\Theta$ in Equation (60). However, the parameter uncertainties estimated from the white noise assumption

$$C_w = \left(\frac{1}{\sigma_{w,\text{eff}}^2} \mathcal{M}^T \mathcal{M} \right)^{-1}, \quad (65)$$

is different from the correct one given in Equation (61). Though by definition, $\sigma_{w,\text{eff}}^2$ is estimated from the data and can be different for each noise realization, for our purpose, it is sufficient to use the noise-averaged value

$$\langle \sigma_{w,\text{eff}}^2 \rangle = \frac{\langle \delta t^T \mathcal{Q}^T \mathcal{Q} \delta t \rangle}{N_{\text{TOA}} - N_{\text{param}}} = \frac{\text{Tr}(\mathcal{C} \mathcal{Q}^T \mathcal{Q})}{N_{\text{TOA}} - N_{\text{param}}}, \quad (66)$$

where

$$\mathcal{Q} = \mathcal{I} - \mathcal{M} (\mathcal{M}^T \mathcal{M})^{-1} \mathcal{M}^T, \quad (67)$$

with \mathcal{I} the identity matrix. Further, the estimation in Equation (67) even does not represent the true covariance of $\delta\Theta_w$ as

$$\langle \delta\Theta_w \delta\Theta_w^T \rangle = (\mathcal{M}^T \mathcal{M})^{-1} \mathcal{M}^T \mathcal{C} \mathcal{M} (\mathcal{M}^T \mathcal{M})^{-1}, \quad (68)$$

while one can easily verify that Equation (61) is consistent with Equation (60), and $C = \langle \delta\Theta \delta\Theta^T \rangle$.

In Figure 6 (b), we show the estimated measurement precision of the mass of SMBH as a function of the red noise amplitude. We show the results both from a correct estimation given by Equation (61), which requires the knowledge of the noise covariance matrix \mathcal{C} , and the estimation based on the assumption of purely white noise as given in Equation (65). However, as we mentioned above, Equation (65) does not correctly give the uncertainty of the best-fit parameter $\delta\Theta_w$. Therefore, we also show the true uncertainty of $\delta\Theta_w$ given by Equation (68). The solid line and dashed line in the figure show the results for two pulsar-SMBH systems that have $P_b = 0.5$ yr and $P_b = 2$ yr respectively. Other system parameters are the same as in Section 2.

From the figure, one can see that, with full knowledge of the noise properties, the parameter estimation uncertainty does not increase a lot even when the red noise has a large amplitude, while the two estimations based on the white noise assumption are largely affected by the presence of red noise. This is because that by assuming a purely white noise, the noise power is incorrectly absorbed by the timing model parameters, and leads to a larger deviation that depends on the noise realization.

More importantly, the figure suggests that assuming a purely white noise also leads to a wrong estimation of the real parameter uncertainty. One can only use Equation (65) as the estimator, as the correct estimation in Equation (68) again requires the knowledge of \mathcal{C} . From the figure, one can see that the estimation in Equation (65) significantly underestimates the parameter uncertainties, which might lead to a false alarm, for example, in deviation of GR when testing gravity. Therefore, careful treatment of the parameter estimation in the presence of red noise is necessary in pulsar-SMBH systems.

4.4. Bayesian approach to parameter estimation

The discussion above suggests that it is necessary to consider the possible red noise in pulsar-SMBH systems. However, in real observations, the noise properties are *a priori* unknown and need to be estimated from the data. In this subsection, we study the effects of red noise in parameter estimations for pulsar-SMBH systems based on the Bayesian approach which is well developed and widely used in pulsar timing (Lentati et al. 2013; Agazie et al. 2023; Chen et al. 2025). Such an approach can estimate the red noise parameters from the timing data simultaneously with other parameters.

For convenience, we first introduce the approach mainly following Lentati et al. (2013). Based on the Bayes' theorem, the posterior for the system parameters Θ , the noise parameters Ξ , and a set of auxiliary noise variables ϵ that will be introduced later, can be written as

$$P(\Theta, \Xi, \epsilon | t^{\text{TOA}}) \propto P(\delta t | \delta\Theta, \Xi, \epsilon) P(\delta\Theta, \Xi, \epsilon) \quad (69) \\ \propto P(\delta t | \delta\Theta, \epsilon) P(\epsilon | \Xi) P(\delta\Theta) P(\Xi),$$

where we have assumed that a primary fit has deduced t^{TOA} and Θ to δt and $\delta\Theta$ respectively. The proportion symbol “ \propto ” used in this subsection exactly means a normalization factor. With linear approximation, the probability function of the pre-fit residual δt , given $\delta\Theta$ and ϵ , reads

$$P(\delta t | \delta\Theta, \epsilon) \propto \frac{\exp \left[-\frac{1}{2} (\mathcal{R} - \mathcal{F}\epsilon)^T C_w^{-1} (\mathcal{R} - \mathcal{F}\epsilon) \right]}{\sqrt{\det C_w}} \quad (70)$$

with $\mathcal{R} = \delta t - \mathcal{M}\delta\Theta$ given in Equation (53). The matrix \mathcal{F} is a set of Fourier bases that aim to account for the red noise component in the pre-fit residual δt , and therefore ϵ gives the mode amplitude. We set

$$\mathcal{F}_{i,l} = \cos(2\pi t_i^{\text{TOA}} l / T_{\text{obs}}), \\ \mathcal{F}_{i,k+l} = \sin(2\pi t_i^{\text{TOA}} l / T_{\text{obs}}), \quad (71)$$

with $i = 1, \dots, N_{\text{TOA}}$, and $l = 1, \dots, k$. The number k , as a hyperparameter, determines the frequency band

that we want to remove the red noise, and its optimal value will be determined later. Finally, C_w in Equation (70) is the noise covariance matrix of purely white noise, as we have explicitly subtracted the red noise component by $\mathcal{F}\epsilon$. As per convention (Chen et al. 2025), we add a multiplicative factor EFAC to Equation (56) as

$$C_w = \text{EFAC}^2 \sigma_{\text{TOA}}^2 \mathcal{I}, \quad (72)$$

and fix $\sigma_{\text{TOA}}^2 = 1$ ms. For real data analysis, one may similarly include all three factors, i.e., EFAC, EQUAD, and ECORR.

$P(\epsilon|\Xi)$ describes the probability of the amplitudes ϵ given the noise parameters. Therefore we have

$$P(\epsilon|\Xi) \propto \frac{1}{\sqrt{\det \varphi}} \exp\left(-\frac{1}{2}\epsilon^T \varphi^{-1} \epsilon\right), \quad (73)$$

where

$$\varphi_{ij} = \langle \epsilon_i \epsilon_j \rangle = \frac{2}{T_{\text{obs}}} P_r(f_i|\Xi) \delta_{ij}. \quad (74)$$

The function P_r is the red noise spectrum that depends on the noise parameters Ξ , and

$$f_i = f_{i+k} = i/T_{\text{obs}}, \quad (75)$$

is the corresponding frequency. Note that the factor “2” in Equation (74) comes from the convention that we are using the two-sided power spectrum.

According to the power-law model of the red noise, we choose

$$P_r(f|\Xi) = \tilde{A} T_{\text{obs}}^3 (f T_{\text{obs}})^{-\alpha}, \quad (76)$$

where \tilde{A} is the dimensionless amplitude defined by $\tilde{A} = A T_{\text{obs}}^{-3} (f_c T_{\text{obs}})^\alpha$. We treat both \tilde{A} and α as noise parameters. Together with EFAC we have

$$\Xi = \{\text{EFAC}, \tilde{A}, \alpha\}. \quad (77)$$

We shall point out that, if one adopts the red-noise model with a low frequency cutoff as in Equation (49), one may not introduce the Fourier components and can directly model the red noise effects with C_r (van Haasteren & Levin 2013). The two methods should provide consistent results. The approach we adopted here has the advantage that we do not need to model the red noise spectrum for low frequencies.

The priors of $\delta\Theta$ and Ξ are given by $P(\delta\Theta)$ and $P(\Xi)$ respectively. As we use the linear approximation, it is natural to choose $P(\delta\Theta)$ to be the flat prior, and we will not discuss it from now on. For the noise parameters, we set $\text{EFAC} \sim \mathcal{U}(0.1, 10)$, $\log_{10} \tilde{A} \sim \mathcal{U}(-30, -10)$, and $\alpha \sim \mathcal{U}(0, 10)$ with \mathcal{U} denoting the uniform distribution (Chen et al. 2025).

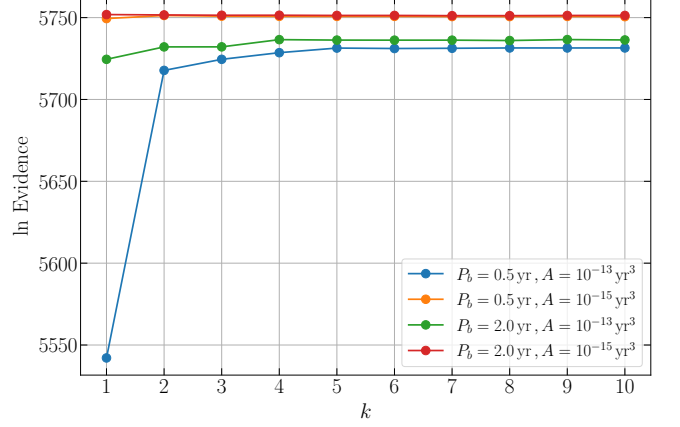


Figure 7. The evidence for four examples as functions of the Fourier bases number k .

As studied by Lentati et al. (2013) and van Haasteren & Levin (2013), for estimating the red noise parameter Ξ , one can analytically marginalize over the Fourier amplitudes ϵ and the timing parameters $\delta\Theta$ when under the assumption of a flat prior. Integrating over ϵ gives

$$P(\delta\Theta, \Xi|\delta t) \propto P(\Xi) \frac{\exp\left[-\frac{1}{2}(\mathcal{R}^T C_w^{-1} \mathcal{R} - d^T \Sigma^{-1} d)\right]}{\sqrt{\det \varphi \det C_w \det \Sigma}}, \quad (78)$$

where

$$d = \mathcal{F}^T C_w^{-1} \mathcal{R}, \quad (79)$$

$$\Sigma = \mathcal{F}^T C_w^{-1} \mathcal{F} + \varphi^{-1}. \quad (80)$$

Further marginalizing $\delta\Theta$ gives us a simple formula that can be used to directly sample the posterior of the noise parameters,

$$P(\Xi|\delta t) \propto P(\Xi) \frac{\exp\left(-\frac{1}{2}\delta t^T \mathcal{X} \delta t\right)}{\sqrt{\det \varphi \det C_w \det \Sigma \det(\mathcal{M}^T \mathcal{Y} \mathcal{M})}}, \quad (81)$$

where

$$\mathcal{Y} = C_w^{-1} - C_w^{-1} \mathcal{F} \Sigma^{-1} \mathcal{F}^T C_w^{-1}, \quad (82)$$

$$\mathcal{X} = \mathcal{Y} - \mathcal{Y} \mathcal{M} (\mathcal{M}^T \mathcal{Y} \mathcal{M})^{-1} \mathcal{M}^T \mathcal{Y}. \quad (83)$$

For numerical stability, one may first perform a singular value decomposition on the design matrix such that $\mathcal{M} = U S V^T$.⁵ Then one has

$$\mathcal{X} = \mathcal{Y} - \mathcal{Y} U (U^T \mathcal{Y} U)^{-1} U^T \mathcal{Y}, \quad (84)$$

and

$$\det(\mathcal{M}^T \mathcal{Y} \mathcal{M}) = \det(U^T \mathcal{Y} U) \det S^2. \quad (85)$$

⁵ Here we adopt the convention that S and V are square matrices.

Note that the term $\det \mathcal{S}^2$ can be dropped as it is a constant that does not depend on Ξ .

With the above formulae, and the same noise injection shown in Figure 6, we perform nested sampling parameter estimation with the `dynesty` sampler in the `BILBY` package (Ashton et al. 2019) to obtain the samples of the posterior $P(\Xi|\delta t)$. We consider four cases that have pulsar's orbital periods $P_b = 0.5 \text{ yr}$ or $P_b = 2.0 \text{ yr}$, and red noise amplitude $A = 10^{-13} \text{ yr}^3$ or $A = 10^{-15} \text{ yr}^3$. For all these cases, we perform 10 samplings with k varying from 1 to 10. The evidences estimated by the sampler are shown in Figure 7. From the figure, one can see that, for the stronger red noise, $A = 10^{-13} \text{ yr}^3$, the evidences increase before about $k = 5$ for both cases, which suggests that including more Fourier components better models the noise. For the cases where the red noise is comparable to the white noise, the increase in k does not significantly change the evidence, which implies that it will be hard to estimate the red noise parameters, especially the spectrum index α . One can also notice that, when the pulsar has a larger orbital period, the change in evidence caused by the modeling of red noise is smaller, as we expect that the timing model will absorb more red noise power when the pulsar's orbital period is larger.

Figure 8 shows the posteriors of the red-noise parameters for the four examples. For all cases and later analysis, we choose $k = 6$ according to previous discussions. But we note that k may vary in other cases and needs to be estimated as above. From the figure, one can see that, as expected, when the red noise is strong, one can extract the red noise parameters from the timing residuals. But for weak noise cases, though the red noise amplitude can be estimated, the spectrum indices are harder to measure, especially for short observation time spans, similar to the case of measuring the stochastic gravitational wave background (Janssen et al. 2015).

To better study the statistical property of the red noise estimation, we generate $N_r = 10000$ noise realizations for $A = 10^{-13} \text{ yr}^3$. Limited by the computational resources, instead of performing the Bayesian analysis, we directly minimize the likelihood function $P(\Xi|\delta t)/P(\Xi)$ based on Equation (81) to obtain the best-fit values Ξ_b of the red noise parameters. Note that minimizing this likelihood is assuming a generalized flat prior instead of the uniform distribution in a finite range that we used before. Nevertheless, they are the same as long as the best-fit point is inside the prior range.

In Figure 9 (a), we show the mean and variance of the best-fit parameters as functions of the pulsar orbital period for the $A = 10^{-13} \text{ yr}^3$ case. As shown in the figure, for each parameter, the deviation of the mean from its true value is well below the variance, which suggests

that the parameter estimation result is practically unbiased. Further, one can see that the variances of the two red noise parameters are increasing for $P_b \gtrsim 1 \text{ yr}$, which is consistent with our previous discussion. Also, the variance calculated here can be regarded as an estimation of the measurement precision of the red noise parameters.

After estimating the red noise parameters, one can easily recover the posteriors of the full parameter set using the resampling technique, which is widely used in many areas (see e.g., Thrane & Talbot 2019; Dong et al. 2025). To recover the posterior of $\delta\Theta$ and Ξ in Equation (78), one may simply draw a corresponding sample of $\delta\Theta$ for each Ξ sample obtained in the previous nested sampling process. The probability function for the resampling is

$$P(\delta\Theta|\Xi, \delta t) \propto \exp \left[-\frac{1}{2} (\delta\Theta - \delta\Theta_b)^T \mathcal{M}^T \mathcal{Y} \mathcal{M} (\delta\Theta - \delta\Theta_b) \right], \quad (86)$$

where

$$\delta\Theta_b = (\mathcal{M}^T \mathcal{Y} \mathcal{M})^{-1} \mathcal{M}^T \mathcal{Y} \delta t, \quad (87)$$

gives the best-fit values of the timing parameters. Figure 10 shows the recovered posterior of the noise parameters as well as the M , χ , q parameters of the SMBH. We find no clear correlation between the noise parameters and the timing parameters, including those that are not shown in the figure. Nevertheless, the above discussions show a practical approach that can estimate the noise parameters and timing parameters simultaneously.

As before, to better understand the statistical properties of the red-noise effects in the parameter estimation of pulsar-SMBH systems, we obtain the best-fit timing parameters for $N_r = 10000$ noise realizations based on Equation (87) and the corresponding best-fit noise parameters. In Figure 9 (b), we show the fractional precision of the SMBH parameters as functions of the pulsar orbital period in the presence of red noise. For comparison, we show the results for three cases: (i) estimate the timing parameters and noise parameters simultaneously; (ii) estimate the timing noise only and assume that we know the true parameters of red noise; (iii) absence of red noise as discussed in Section 3. One can clearly see that the presence of red noise will increase the parameter estimation uncertainty, especially for pulsars in larger orbits. As expected, the curve represents the case in which we know the red noise parameters are between two case (i) and case (iii). However, even for a red noise that is relatively large, for example $A = 10^{-13} \text{ yr}^3$ considered in this figure, if one treats it properly, the increase of the measurement precision is mild, especially

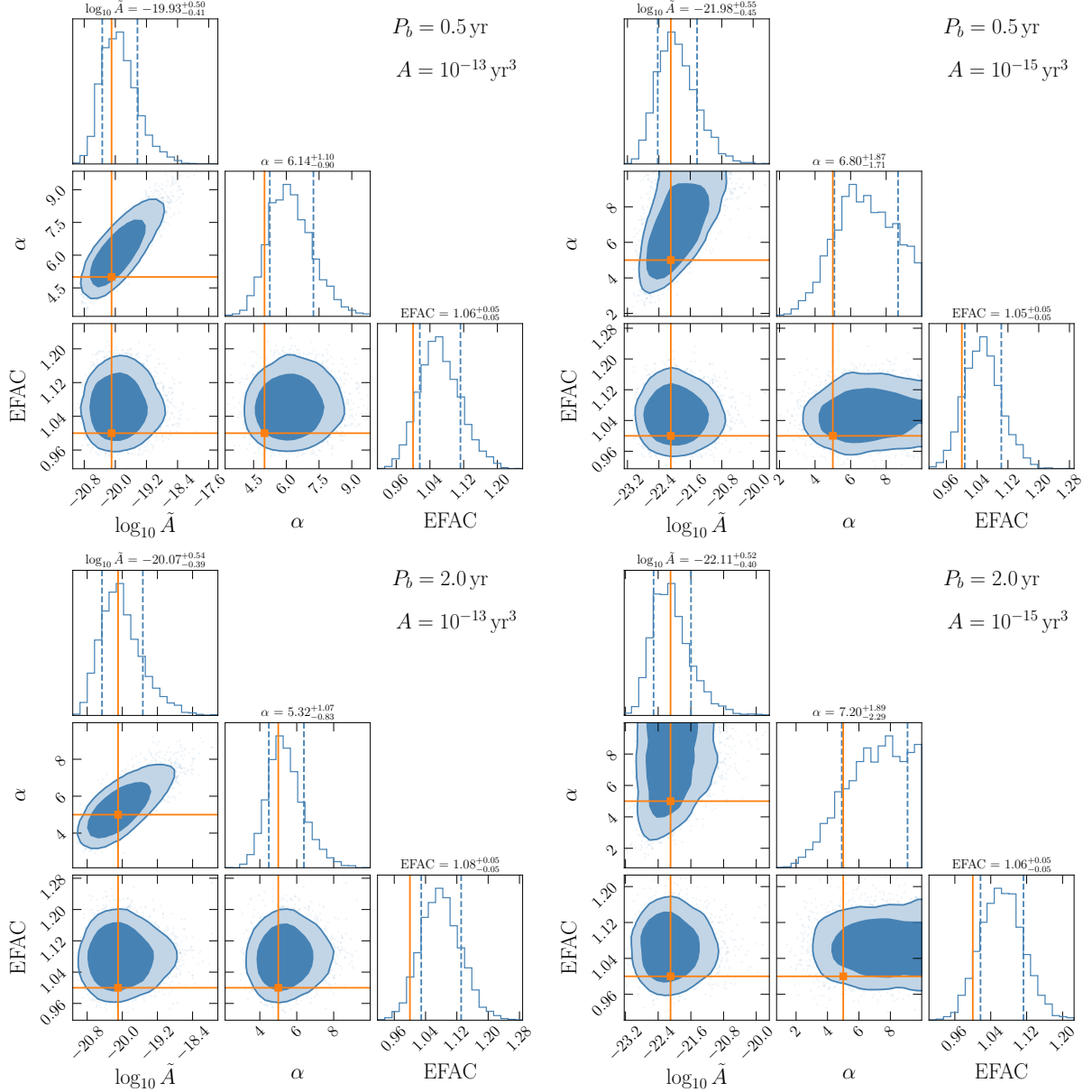


Figure 8. Posteriors of red-noise parameter for four cases with different pulsar orbital periods and red noise amplitudes. The number of Fourier bases is $k = 6$ for all these figures. The true values of the parameters are marked by the orange lines and squares. The dashed lines show the 1- σ intervals of the 1-D marginalized distributions, while the contours show the 68% and 90% credible regions in the 2-D parameter space.

for pulsars with orbital period $P_b \lesssim T_{\text{obs}}/10$. In contrast, improper treatments, as shown in Figure 6 (b), may cause larger biases in the results of parameter estimation.

We shall also note that, in the presence of a red noise with a shallower spectrum, for example, red noise caused by the DM variation, the estimation of timing parameters for pulsars in smaller orbits might also be affected, as more noise power will leak into the frequency of orbital motion.

Finally, another common way of dealing with timing red noise is to include higher-order spin derivatives in the pulsar’s rotation model (21). For example, in the data analysis of the double pulsar, up to fourth order spin derivatives were considered (Kramer et al. 2021). In principle, the higher-order spin derivatives will absorb part of the red noise, as in the frequency domain, fitting these parameters effectively applies a high-pass filter to the power spectrum of the timing residual. Nevertheless,

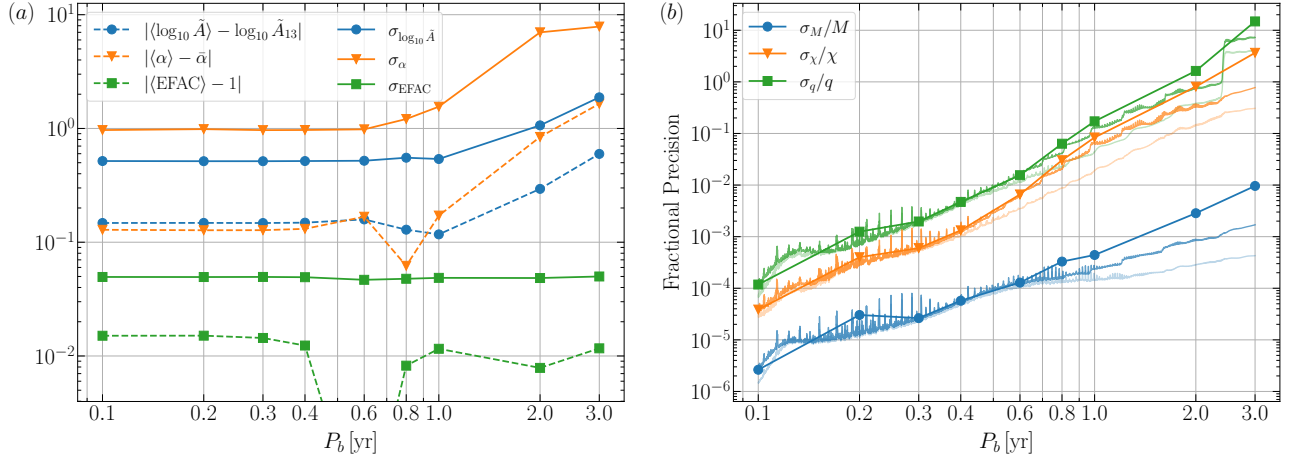


Figure 9. (a) The absolute difference between the averaged values of the best-fit noise parameters and true parameters, as well as the standard deviation of the best-fit parameters for $N_r = 10000$ noise realizations. In this figure we have used $\tilde{A}_{13} = 8 \times 10^{-21}$ and $\bar{\alpha} = 5$. (b) The fractional precision of SMBH parameters as functions of the pulsar orbital period in the presence of red noise. We have used $A = 10^{-13} \text{ yr}^3$ and $\alpha = 5$. The points are the variance of the best-fit parameters in $N_r = 10000$ noise realizations, while the fainter lines are the parameter estimation results assuming that we know the true noise parameters or do not consider the red noise (see the same line in Figure 4 (b)).

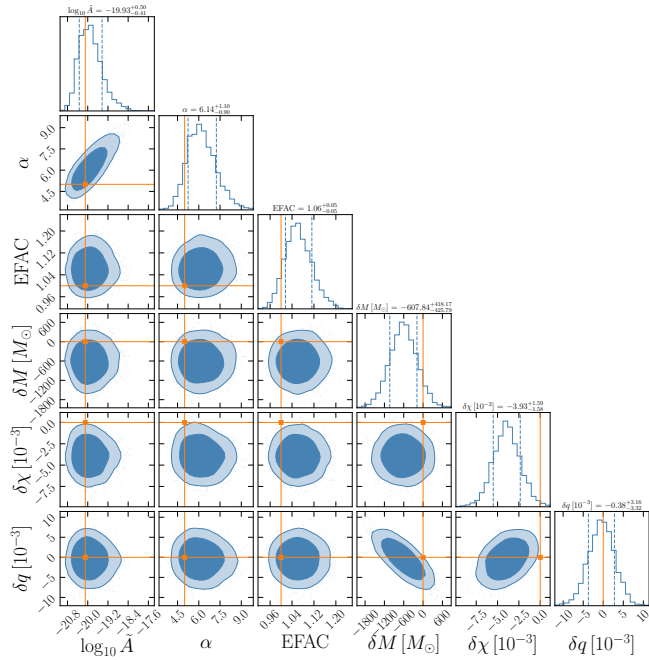


Figure 10. The recovered posterior for the $P_b = 0.5 \text{ yr}$ and $A = 10^{-13} \text{ yr}^3$ case shown before. We only show the posteriors of the noise parameters, and M , χ , q of the SMBH. No clear correlation between noise parameters and timing parameters is found.

we still suggest to perform full noise analysis for pulsar-SMBH systems when possible.

5. CONCLUSIONS

In this work, we construct a realistic pulsar-SMBH timing model based on numerically integrating the PN equations of motion. We give a comprehensive discussion of all the effects that need to be taken into account in the pulsar's orbital motion and light propagation, including several next-to-leading-order effects and the proper motion of Sgr A*, which were not considered in previous studies (except for Zhang & Saha 2017, which adopted a fully GR approach that intrinsically includes all the effects but less extensible).

Based on our timing model, we are able to first discuss the effects of the proper motion of Sgr A*. We find that the current VLBA observation already provides a proper-motion measurement that is accurate than what is possible from timing measurement, which suggests that we can treat the proper motion of Sgr A* as fixed parameters when performing parameter estimation. This enables us to measure the longitude of the ascending node Ω of the pulsar's orbit. However, we find that the constraint on Ω is rather weak, especially for pulsars with small orbits. Therefore, taking into account the proper motion of Sgr A* might not significantly break the leading-order degeneracy in spin measurement, which is in contrast to the prospects in Zhang & Saha (2017).

We also for the first time discuss the aberration effects in such systems. The aberration effects are related to the spin of the pulsar. Due to the relatively long spin-precession time scale in these systems, we treat the pulsar's spin vector as constant in our investigation. We give the expression of the next-to-leading-order aberration

tion time delay and find that it might be relevant for pulsars in compact orbits. According to our parameter estimation result, based on timing-only observation, one might be able to constrain the direction of the pulsar's rotation axis to ~ 1 rad level for pulsars with orbital periods $P_b \lesssim 0.5$ yr.

Using this comprehensive timing model, we give a detailed discussion of the parameter estimation for pulsar-SMBH systems. We consider the parameter estimation in the presence of red noise. Differently from usual binary pulsar systems, the red noise may affect the estimation of the orbital parameters due to the large orbital timing scale of pulsar-SMBH systems. Our results suggest that, even for relatively strong red noise, treating it properly only leads to a mild increase in the uncertainties of parameters, especially for pulsars with orbital periods $P_b \lesssim T_{\text{obs}}/10$. However, improper treatment, like counting the red noise as effective white noise, may lead to significant biases for parameter estimation. Worth to

note that, in the current study, we only consider a red noise with spectrum index $\alpha = 5$, which is typical for the intrinsic red noise of normal pulsars. However, red noise with a shallower spectrum, for example, red noise caused by unmodeled dispersion-measure variation, may cause a larger influence for pulsars with shorter orbital periods.

- 1 We thank Norbert Wex for helpful discussions, and
- 2 Matthew Bailes for raising the question about red
- 3 noise. This work was supported by the National Natu-
- 4 ral Science Foundation of China (124B2056, 123B2043,
- 5 12573042), the National SKA Program of China
- 6 (2020SKA0120300), the Beijing Natural Science Foun-
- 7 dation (1242018), the Max Planck Partner Group Pro-
- 8 gram funded by the Max Planck Society, and the High-
- 9 performance Computing Platform of Peking University.

APPENDIX

A. NEXT-TO-LEADING-ORDER ABERRATION DELAY

Here, we give a brief derivation of the aberration delay that is fully caused by the orbital motion of the pulsar and special relativity to the next-to-leading order. Consider that at the instant when the pulsar emits a pulse towards the Earth, the pulsar has an orbital velocity \mathbf{v} . The light emitted by the pulsar in the direction of $-\hat{\mathbf{K}}'_0$ seen in the proper frame of the pulsar needs to point towards $-\hat{\mathbf{K}}_0$ in the center of mass frame of the pulsar-SMBH system in order to reach the Earth. The velocity transformation formula in special relativity thus gives us

$$\begin{aligned} -\hat{\mathbf{K}}'_0 &= -\hat{\mathbf{K}}_0 - \left(\frac{\hat{\mathbf{K}}_0 \cdot \hat{\mathbf{v}} + v/c}{1 + \hat{\mathbf{K}}_0 \cdot \mathbf{v}/c} - \hat{\mathbf{K}}_0 \cdot \hat{\mathbf{v}} \right) \hat{\mathbf{v}} - [\hat{\mathbf{K}}_0 - (\hat{\mathbf{K}}_0 \cdot \hat{\mathbf{v}})\hat{\mathbf{v}}] \left(\frac{\sqrt{1 - v^2/c^2}}{1 + \hat{\mathbf{K}}_0 \cdot \mathbf{v}/c} - 1 \right) \\ &= -\hat{\mathbf{K}}_0 \left\{ 1 - \frac{v}{c}(\hat{\mathbf{K}}_0 \cdot \hat{\mathbf{v}}) + \frac{v^2}{2c^2} [2(\hat{\mathbf{K}}_0 \cdot \hat{\mathbf{v}})^2 - 1] \right\} - \frac{\mathbf{v}}{c} \left[1 - \frac{v}{2c}(\hat{\mathbf{K}}_0 \cdot \hat{\mathbf{v}}) \right] + O\left(\frac{v}{c}\right)^3, \end{aligned} \quad (\text{A1})$$

where $\hat{\mathbf{v}} = \mathbf{v}/v$. The expression can be checked with, for example, Equation (7.6) in [Klioner & Kopeikin \(1992\)](#). The aberration delay can be calculated by $\Delta_A = \Delta\Phi/2\pi\nu$, and

$$\sin \Delta\Phi = \hat{\mathbf{e}}_3 \cdot \frac{(-\hat{\mathbf{K}}_0 \times \hat{\mathbf{e}}_3) \times (-\hat{\mathbf{K}}'_0 \times \hat{\mathbf{e}}_3)}{|\hat{\mathbf{K}}_0 \times \hat{\mathbf{e}}_3| \cdot |-\hat{\mathbf{K}}'_0 \times \hat{\mathbf{e}}_3|}. \quad (\text{A2})$$

Keep to the second order in v/c , the above equation then gives

$$\Delta_A = -\frac{1}{2\pi\nu} \frac{\mathbf{v} \cdot (\hat{\mathbf{K}}_0 \times \hat{\mathbf{e}}_3)}{c|\hat{\mathbf{K}}_0 \times \hat{\mathbf{e}}_3|^2} \left(1 + \frac{\mathbf{v} \cdot \hat{\mathbf{K}}_0}{2c} + \frac{\mathbf{v} \cdot [\hat{\mathbf{K}}_0 - (\hat{\mathbf{K}}_0 \cdot \hat{\mathbf{e}}_3)\hat{\mathbf{e}}_3]}{c|\hat{\mathbf{K}}_0 \times \hat{\mathbf{e}}_3|^2} \right). \quad (\text{A3})$$

B. NUMERICAL ACCURACY OF THE TIMING MODEL

In Section 2, we constructed the numerical timing model as well as the inverse timing model. A key question is the numerical accuracy of our treatment, as the data analysis of the pulsar timing observation requires us to track the TOAs with millisecond-level accuracy over the whole observation time span, which usually has a time scale of $\mathcal{O}(10)$ yr. Therefore, here we give a rough estimation of the numerical accuracy of our timing model and the corresponding inverse timing model.

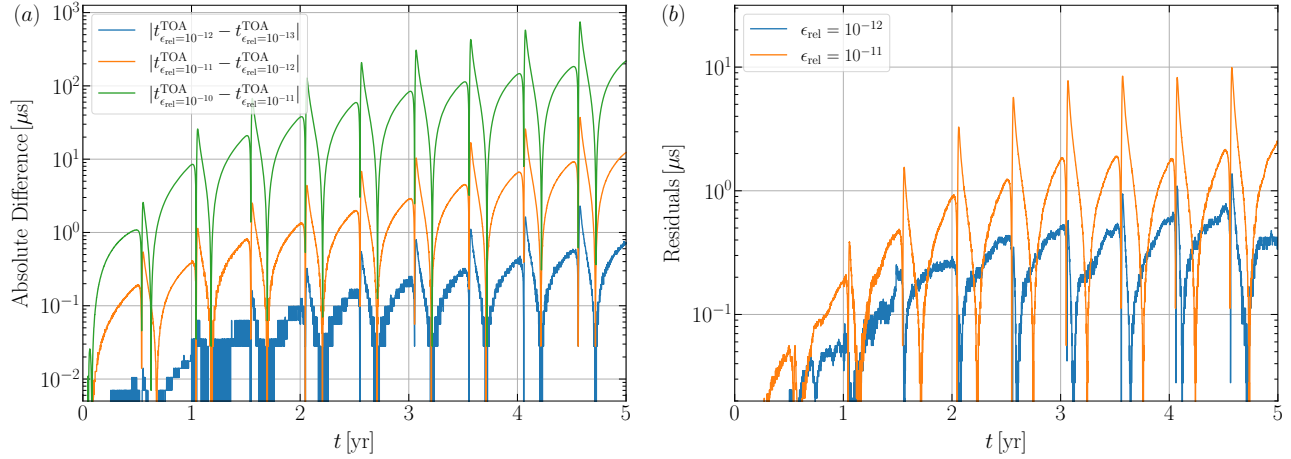


Figure 11. (a) Convergence test of t^{TOA} as a function of t . We choose four different desired relative errors, namely $\epsilon_{\text{rel}} = 10^{-10}$, 10^{-11} , 10^{-12} , and 10^{-13} . One can see a clear convergence among the results. The system parameters used for this figure are the same as the parameters used for Figure 2. (b) The residual caused by cumulated numerical errors in our integration. For a 5-yr simulation, the numerical error is at the order of $1 \mu\text{s}$ and $10 \mu\text{s}$ for $\epsilon_{\text{rel}} = 10^{-12}$ and $\epsilon_{\text{rel}} = 10^{-11}$, respectively. The error level is consistent with panel (a) of this figure.

In our code, to solve the equations of motion for the timing model or the differential equations for the inverse timing model, we use the explicit embedded Runge-Kutta Prince-Dormand (8, 9) method provided in the GSL library (Galassi & Gough 2009), which has adaptive step-size control. Therefore, the step size of the integration is mainly controlled by a parameter called the desired relative error, ϵ_{rel} . In Figure 11 (a), we show a convergence test for t^{TOA} as a function of t , which can be generated from our timing model. We choose four ϵ_{err} , namely 10^{-10} , 10^{-11} , 10^{-12} , and 10^{-13} in our test. The results show a clear convergence. Therefore, the numerical error for our code to generate TOAs during a 5-yr time period can be estimated as, for example, for $\epsilon_{\text{rel}} = 10^{-11}$, at the $10 \mu\text{s}$ level, while for $\epsilon_{\text{rel}} = 10^{-12}$, at the $1 \mu\text{s}$ level. This error is far below the expected timing precision, so that our code is reliable at least for the observation time span considered in this work. Though for a longer time span, one may need to use a smaller ϵ_{rel} , or even use better storage precision as performed in Tempo2 (Hobbs et al. 2006). Considering the consistency with the numerical derivative part to be discussed in Appendix C, in this work, we always set $\epsilon_{\text{rel}} = 10^{-11}$. Though we shall notice that $\epsilon_{\text{rel}} = 10^{-11}$ discussed there in general leads to a smaller integration step size due to the enlargement of the equation set. So that if one only uses the timing model or the inverse timing model, a smaller ϵ_{rel} like $\epsilon_{\text{rel}} = 10^{-12}$ or 10^{-13} is better, but a too small ϵ_{rel} will lead to a large cumulated round-off error due to the small integration step size.

We also investigate the numerical accuracy of the inverse timing model. We simulate a series of TOAs with our timing model and calculate the residuals with the true parameters of the system and the inverse timing model. In principle, this should give us a vanishing result. However, due to the numerical error cumulated in the integration, a non-zero residual will exist as shown in Figure 11 (b). For the 5-yr simulation, the residual caused by numerical error is at the order of $1 \mu\text{s}$ and $10 \mu\text{s}$ for $\epsilon_{\text{rel}} = 10^{-12}$ and $\epsilon_{\text{rel}} = 10^{-11}$, respectively. The error level is consistent with the previous analysis and well below the required precision limit.

C. NUMERICAL DERIVATIVES FOR THE FISHER MATRIX

In Section 3.1, we introduced the Fisher matrix method that we used to estimate the measurement precision of the system parameters. To construct the Fisher matrix, one needs to calculate the first-order derivatives, $\partial \mathcal{N}_i / \partial \Theta^\alpha$, as shown in Equation (47). A usual treatment is to use the finite difference method to calculate this derivative. For example, for the second-order central difference, one has

$$\frac{\partial \mathcal{N}_i}{\partial \Theta^\alpha} \approx \frac{-\mathcal{N}_i(\bar{\Theta}^\alpha + 2h) + 8\mathcal{N}_i(\bar{\Theta}^\alpha + h) - 8\mathcal{N}_i(\bar{\Theta}^\alpha - h) + \mathcal{N}_i(\bar{\Theta}^\alpha - 2h)}{12h}, \quad (\text{C4})$$

where h is the step size of the finite difference. The numerical error in the above equation comes from two aspects. One is the finite difference approximation, as one truncates the Taylor expansion at a finite order. For this second-order formula, the error is proportional to h^5 . Another part of the error budget comes from the fact that the above equation

is performing subtraction for large numbers. For a 5-yr observation time span, the proper rotation number \mathcal{N} of the pulsar can reach about $5\text{ yr}/1\text{ sec} \sim 10^8$. Due to the finite precision of a stored number, this gives an error around $10^{-8}/h$ for the `double precision` we used. Therefore, to obtain the best estimation of the derivatives, one needs to balance these two errors.

The above discussion can be found in standard textbooks of numerical methods. However, we find that, for some parameters in our pulsar-SMBH systems, one cannot find a step size h that gives a satisfactory precision. In general, this happens for angular variables that cannot be measured with high precision. For example, the direction parameters of the SMBH's spin, λ and η . One can roughly think that, for these variables, changing them a lot only introduces a small change in \mathcal{N}_i . Therefore, the error in the above equation mainly comes from the finite storage precision. However, different from those linear parameters like χ or q , for which one can increase the step size to control the error, angular variables cannot have a large step size h as they are periodic over 2π . This leads to a large error in the Fisher matrix calculation.

To avoid the above problem, we use a different method for calculating the derivatives. Taking λ as an example, one may notice that

$$\frac{\partial \mathcal{N}_i}{\partial \lambda} = (\nu + \dot{\nu} T_i + \dots) \frac{\partial T_i}{\partial \lambda}, \quad (\text{C5})$$

where $T_i = t_i - \Delta_E(t_i)$ is the corresponding emission time of the pulse. To calculate $\partial t_i/\partial \lambda$ or $\partial \Delta_E/\partial \lambda$, one can rely on the continuous dependence of the solutions of ordinary differential equations on their parameters. That is, denoting the equations of motion for pulsar timing as

$$\frac{\partial \mathbf{X}}{\partial t^{\text{TOA}}} = \mathbf{f}[\mathbf{X}(\lambda), \lambda], \quad (\text{C6})$$

where \mathbf{X} denotes the parameter set $\{\mathbf{r}, \mathbf{v}, t, \Delta_E\}$. One can take a derivative of λ for the above equation and obtain

$$\frac{\partial}{\partial t^{\text{TOA}}} \frac{\partial \mathbf{X}}{\partial \lambda} = \frac{\partial \mathbf{f}}{\partial \mathbf{X}} \frac{\partial \mathbf{X}}{\partial \lambda} + \frac{\partial \mathbf{f}}{\partial \lambda}. \quad (\text{C7})$$

The above equation, together with the original equations of motion of the pulsar, form a complete differential system that can be used to solve $\partial t/\partial \lambda$. One can also take the derivative of the original initial conditions to obtain the initial conditions needed here. All the derivatives needed for constructing the above equation can be done analytically, and as a whole, it avoids the problem of subtraction of large numbers. Therefore, this method can give a much accurate calculation for the derivatives we want. This method also speeds up the calculation for the Fisher matrix a bit, as the finite difference method requires calculating the orbital integration four times for each parameter.

In Figure 12 (a), we show a comparison of the parameter estimation results obtained from two methods. The dashed lines are obtained with the finite difference method where we have fine-tuned the step size for each parameter to obtain the best result, while the solid lines employ the method we discussed above. All system parameters for the two cases are the same. In this figure, for each line, we calculate 5000 points so that one can see small structures clearly. For example, one may notice that there are a lot of spikes in both results. These spikes are real and come from the whole integer ratio of the pulsar's orbital period and the observation cadence (one week). That is, all the main peaks roughly locate around $P_b = k/52\text{ yr}$, with k an integer, while smaller peaks allow k to be a half-integer or other rational numbers. Though for real observations, due to the more complex observation cadence, one should not expect a pulsar-SMBH system to be located exactly in such a peak. Similarly, around $P_b = 2.5\text{ yr}$, one can see a step-like behavior which comes from the fact that an additional periastron passage is observed during the 5-yr time span.

However, beside these clean structures, when the pulsar has an orbital period $P_b \gtrsim 1\text{ yr}$, one can see strong oscillations in the dashed lines, especially for the spin parameter χ . This indeed comes from numerical errors in calculating the derivatives. As discussed before, when the measurement precision is poor, the derivative calculations for the spin direction, described by λ and η , are also problematic. One can see that the method proposed here suppresses these oscillations, and we think it provides a more reliable result. Also, as partially discussed in Section 3.3, the different trends in the two sets of results are due to the correct resolution of the proper motion effects, which are related to parameter Ω that is also a poorly constrained angular variable.

Instead of the step size h for the finite difference calculation, the method we proposed here is somehow controlled by the step size for the integration of the differential equations. As mentioned before, in our code, we use the explicit embedded Runge-Kutta Prince-Dormand (8, 9) method provided in the GSL library (Galassi & Gough 2009), which has

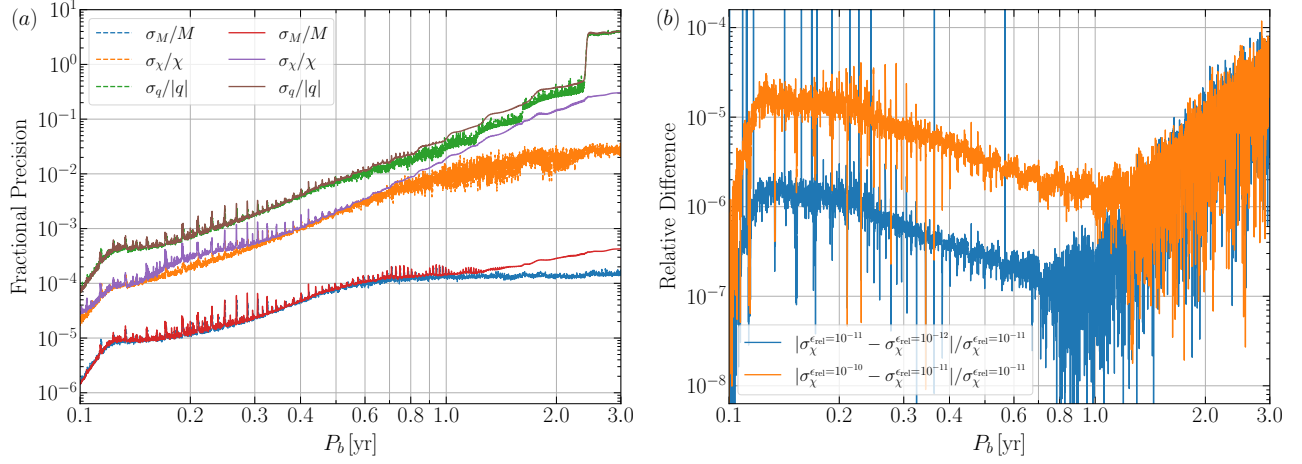


Figure 12. (a) Comparison of the parameter estimation results obtained with two different methods. The dashed lines employ the finite difference method, while the solid lines are based on solving the differential equations. One clearly sees that, when the pulsar’s orbital periods are large, which leads to a worse measurement precision, the numerical errors in the results are largely suppressed with the method we proposed. (b) Convergence test of the parameter estimation results for the spin parameter χ . In these results, we calculate the numerical derivatives using the new method proposed here. The desired relative errors ϵ_{rel} for the convergence test are chosen to be 10^{-10} , 10^{-11} , and 10^{-12} , respectively. The system parameters used for this figure are the same as the parameters used for Figure 2.

adaptive step-size control. The parameter we can adjust is the desired relative error ϵ_{rel} for the integration. To further verify our method, by using different ϵ_{rel} , we perform a convergence test of our parameter estimation results. We set the desired relative error ϵ_{rel} to 10^{-10} , 10^{-11} , and 10^{-12} , and perform full parameter estimations. Figure 12 (b) shows the relative difference of the parameter estimation results for the spin parameter χ . One can see a clear convergence for $P_b \lesssim 1$ yr, while for a larger P_b , the numerical error may be dominated by the round-off error in the numerical integration. Note that a smaller desired relative error will lead to a smaller step size and therefore more floating-point arithmetic, so that the blue curve has a larger part that is dominated by this error. Nevertheless, the overall relative error in our calculation is less than 10^{-4} , and the finite step-size error seems to be balanced with the round-off error for $\epsilon_{\text{rel}} = 10^{-11}$. Therefore, in the main text, we always use this setup. Finally, the small relative difference also suggests that the spikes in the results discussed before are physical and being correctly resolved, as their values are also insensitive to the numerical setup.

REFERENCES

- Abac, A. G., et al. 2025a, *Astrophys. J. Lett.*, 995, L18, doi: [10.3847/2041-8213/ae0c06](https://doi.org/10.3847/2041-8213/ae0c06)
- . 2025b. <https://arxiv.org/abs/2508.18082>
- Abbate, F., et al. 2025, *Open J. Astrophys.*, 8, 54252, doi: [10.33232/001c.154252](https://doi.org/10.33232/001c.154252)
- Abbott, B. P., et al. 2016a, *Phys. Rev. Lett.*, 116, 061102, doi: [10.1103/PhysRevLett.116.061102](https://doi.org/10.1103/PhysRevLett.116.061102)
- . 2016b, *Phys. Rev. Lett.*, 116, 221101, doi: [10.1103/PhysRevLett.116.221101](https://doi.org/10.1103/PhysRevLett.116.221101)
- Abuter, R., et al. 2020, *Astron. Astrophys.*, 636, L5, doi: [10.1051/0004-6361/202037813](https://doi.org/10.1051/0004-6361/202037813)
- Agazie, G., et al. 2023, *Astrophys. J. Lett.*, 951, L8, doi: [10.3847/2041-8213/acdac6](https://doi.org/10.3847/2041-8213/acdac6)
- Akiyama, K., et al. 2022, *Astrophys. J. Lett.*, 930, L12, doi: [10.3847/2041-8213/ac6674](https://doi.org/10.3847/2041-8213/ac6674)
- . 2024, *Astrophys. J. Lett.*, 964, L26, doi: [10.3847/2041-8213/ad2df1](https://doi.org/10.3847/2041-8213/ad2df1)
- Ashton, G., et al. 2019, *Astrophys. J. Suppl.*, 241, 27, doi: [10.3847/1538-4365/ab06fc](https://doi.org/10.3847/1538-4365/ab06fc)
- Barker, B. M., & O’Connell, R. F. 1974, *Gen. Relativ. Gravit.*, 5, 539, doi: [10.1007/BF02451397](https://doi.org/10.1007/BF02451397)
- . 1975, *Phys. Rev. D*, 12, 329, doi: [10.1103/PhysRevD.12.329](https://doi.org/10.1103/PhysRevD.12.329)
- . 1979, *Gen. Relativ. Gravit.*, 11, 149, doi: [10.1007/BF00756587](https://doi.org/10.1007/BF00756587)
- Blandford, R., & Teukolsky, S. A. 1976, *Astrophys. J.*, 205, 580, doi: [10.1086/154315](https://doi.org/10.1086/154315)
- Bower, G. C., et al. 2018, *ASP Conf. Ser.*, 517, 793. <https://arxiv.org/abs/1810.06623>

- Caballero, R. N., et al. 2016, *Mon. Not. Roy. Astron. Soc.*, 457, 4421, doi: [10.1093/mnras/stw179](https://doi.org/10.1093/mnras/stw179)
- Carter, B. 1971, *Phys. Rev. Lett.*, 26, 331, doi: [10.1103/PhysRevLett.26.331](https://doi.org/10.1103/PhysRevLett.26.331)
- Chen, S., et al. 2025, *Astron. Astrophys.*, 699, A165, doi: [10.1051/0004-6361/202452550](https://doi.org/10.1051/0004-6361/202452550)
- Cieřlik, A., Hackmann, E., & Mach, P. 2023, *Phys. Rev. D*, 108, 024056, doi: [10.1103/PhysRevD.108.024056](https://doi.org/10.1103/PhysRevD.108.024056)
- Coles, W., Hobbs, G., Champion, D. J., Manchester, R. N., & Verbiest, J. P. W. 2011, *Mon. Not. Roy. Astron. Soc.*, 418, 561, doi: [10.1111/j.1365-2966.2011.19505.x](https://doi.org/10.1111/j.1365-2966.2011.19505.x)
- Cordes, J. M., & Lazio, T. J. W. 2002. <https://arxiv.org/abs/astro-ph/0207156>
- Damour, T., & Deruelle, N. 1986, *Ann. Inst. Henri Poincaré Phys. Théor.*, 44, 263
- Damour, T., & Schaefer, G. 1988, *Nuovo Cim. B*, 101, 127, doi: [10.1007/BF02828697](https://doi.org/10.1007/BF02828697)
- Damour, T., & Taylor, J. H. 1992, *Phys. Rev. D*, 45, 1840, doi: [10.1103/PhysRevD.45.1840](https://doi.org/10.1103/PhysRevD.45.1840)
- Della Monica, R., & de Martino, I. 2025. <https://arxiv.org/abs/2501.03912>
- Deneva, J. S., Cordes, J. M., & Lazio, T. J. W. 2009, *Astrophys. J. Lett.*, 702, L177, doi: [10.1088/0004-637X/702/2/L177](https://doi.org/10.1088/0004-637X/702/2/L177)
- Desvignes, G., Eatough, R. P., Men, Y., et al. 2026, *Astron. Astrophys.*, 706, A113, doi: [10.1051/0004-6361/202556381](https://doi.org/10.1051/0004-6361/202556381)
- Dexter, J., & O’Leary, R. M. 2014, *Astrophys. J. Lett.*, 783, L7, doi: [10.1088/2041-8205/783/1/L7](https://doi.org/10.1088/2041-8205/783/1/L7)
- Dong, Y., Shao, L., Hu, Z., Miao, X., & Wang, Z. 2022, *JCAP*, 11, 051, doi: [10.1088/1475-7516/2022/11/051](https://doi.org/10.1088/1475-7516/2022/11/051)
- Dong, Y., Wang, Z., Wang, H.-T., Zhao, J., & Shao, L. 2025. <https://arxiv.org/abs/2502.01093>
- Doroshenko, O. V., & Kopeikin, S. M. 1995, *Mon. Not. Roy. Astron. Soc.*, 274, 1029, doi: [10.1093/mnras/274.4.1029](https://doi.org/10.1093/mnras/274.4.1029)
- Eatough, R. P., et al. 2013, *Nature*, 501, 391, doi: [10.1038/nature12499](https://doi.org/10.1038/nature12499)
- Ferdman, R. D., et al. 2013, *Astrophys. J.*, 767, 85, doi: [10.1088/0004-637X/767/1/85](https://doi.org/10.1088/0004-637X/767/1/85)
- Freire, P. C. C., & Wex, N. 2024, *Living Rev. Rel.*, 27, 5, doi: [10.1007/s41114-024-00051-y](https://doi.org/10.1007/s41114-024-00051-y)
- Galassi, M., & Gough, B. 2009, *GNU Scientific Library: Reference Manual*, GNU manual (Network Theory). <http://www.gnu.org/software/gsl/>
- Greenstein, G. 1970, *Nature*, 227, 791, doi: [10.1038/227791a0](https://doi.org/10.1038/227791a0)
- Hackmann, E., & Dhani, A. 2019, *Gen. Rel. Grav.*, 51, 37, doi: [10.1007/s10714-019-2517-2](https://doi.org/10.1007/s10714-019-2517-2)
- Hobbs, G., Edwards, R., & Manchester, R. 2006, *Mon. Not. Roy. Astron. Soc.*, 369, 655, doi: [10.1111/j.1365-2966.2006.10302.x](https://doi.org/10.1111/j.1365-2966.2006.10302.x)
- Hobbs, G., Lyne, A. G., & Kramer, M. 2010, *Mon. Not. Roy. Astron. Soc.*, 402, 1027, doi: [10.1111/j.1365-2966.2009.15938.x](https://doi.org/10.1111/j.1365-2966.2009.15938.x)
- Hu, Z., Miao, X., & Shao, L. 2024a, *Tests of Classical Gravity with Radio Pulsars*, doi: [10.1007/978-981-97-2871-8_3](https://doi.org/10.1007/978-981-97-2871-8_3)
- Hu, Z., & Shao, L. 2024, *Phys. Rev. Lett.*, 133, 231402, doi: [10.1103/PhysRevLett.133.231402](https://doi.org/10.1103/PhysRevLett.133.231402)
- Hu, Z., Shao, L., Xu, R., Liang, D., & Mai, Z.-F. 2024b, *JCAP*, 04, 087, doi: [10.1088/1475-7516/2024/04/087](https://doi.org/10.1088/1475-7516/2024/04/087)
- Hu, Z., Shao, L., & Zhang, F. 2023, *Phys. Rev. D*, 108, 123034, doi: [10.1103/PhysRevD.108.123034](https://doi.org/10.1103/PhysRevD.108.123034)
- Janssen, G., et al. 2015, *PoS, AASKA14*, 037, doi: [10.22323/1.215.0037](https://doi.org/10.22323/1.215.0037)
- Johnston, S., Kramer, M., Lorimer, D. R., et al. 2006, *Mon. Not. Roy. Astron. Soc.*, 373, L6, doi: [10.1111/j.1745-3933.2006.00232.x](https://doi.org/10.1111/j.1745-3933.2006.00232.x)
- Kidder, L. E. 1995, *Phys. Rev. D*, 52, 821, doi: [10.1103/PhysRevD.52.821](https://doi.org/10.1103/PhysRevD.52.821)
- Klioner, S. A., & Kopeikin, S. M. 1992, *Astron. J.*, 104, 897, doi: [10.1086/116284](https://doi.org/10.1086/116284)
- Klioner, S. A., & Zschocke, S. 2010, *Class. Quant. Grav.*, 27, 075015, doi: [10.1088/0264-9381/27/7/075015](https://doi.org/10.1088/0264-9381/27/7/075015)
- Kopeikin, S. M. 1996, *Astrophys. J. Lett.*, 467, L93, doi: [10.1086/310201](https://doi.org/10.1086/310201)
- Kormendy, J., & Ho, L. C. 2013, *Ann. Rev. Astron. Astrophys.*, 51, 511, doi: [10.1146/annurev-astro-082708-101811](https://doi.org/10.1146/annurev-astro-082708-101811)
- Kramer, M., et al. 2021, *Phys. Rev. X*, 11, 041050, doi: [10.1103/PhysRevX.11.041050](https://doi.org/10.1103/PhysRevX.11.041050)
- Lam, M. T., et al. 2017, *Astrophys. J.*, 834, 35, doi: [10.3847/1538-4357/834/1/35](https://doi.org/10.3847/1538-4357/834/1/35)
- Lense, J., & Thirring, H. 1918, *Phys. Z.*, 19, 156
- Lentati, L., Alexander, P., Hobson, M. P., et al. 2013, *Phys. Rev. D*, 87, 104021, doi: [10.1103/PhysRevD.87.104021](https://doi.org/10.1103/PhysRevD.87.104021)
- Lentati, L., et al. 2016, *Mon. Not. Roy. Astron. Soc.*, 458, 2161, doi: [10.1093/mnras/stw395](https://doi.org/10.1093/mnras/stw395)
- Li, K. J., Wu, K., Younsi, Z., Teixeira, J., & Singh, D. 2024, *Mon. Not. Roy. Astron. Soc.*, 530, 1118, doi: [10.1093/mnras/stae883](https://doi.org/10.1093/mnras/stae883)
- Liu, K., Wex, N., Kramer, M., Cordes, J. M., & Lazio, T. J. W. 2012, *Astrophys. J.*, 747, 1, doi: [10.1088/0004-637X/747/1/1](https://doi.org/10.1088/0004-637X/747/1/1)
- Lorimer, D. R., & Kramer, M. 2005, *Handbook of Pulsar Astronomy* (Cambridge, England: Cambridge University Press)

- Lower, M. E., Dai, S., Johnston, S., & Barr, E. D. 2024, *Astrophys. J. Lett.*, 967, L16, doi: [10.3847/2041-8213/ad4866](https://doi.org/10.3847/2041-8213/ad4866)
- Lyne, A., Hobbs, G., Kramer, M., Stairs, I., & Stappers, B. 2010, *Science*, 329, 408, doi: [10.1126/science.1186683](https://doi.org/10.1126/science.1186683)
- Manchester, R. N., Hobbs, G. B., Teoh, A., & Hobbs, M. 2005, *Astron. J.*, 129, 1993, doi: [10.1086/428488](https://doi.org/10.1086/428488)
- McConnell, N. J., & Ma, C.-P. 2013, *Astrophys. J.*, 764, 184, doi: [10.1088/0004-637X/764/2/184](https://doi.org/10.1088/0004-637X/764/2/184)
- Merritt, D., Alexander, T., Mikkola, S., & Will, C. M. 2010, *Phys. Rev. D*, 81, 062002, doi: [10.1103/PhysRevD.81.062002](https://doi.org/10.1103/PhysRevD.81.062002)
- Parthasarathy, A., et al. 2019, *Mon. Not. Roy. Astron. Soc.*, 489, 3810, doi: [10.1093/mnras/stz2383](https://doi.org/10.1093/mnras/stz2383)
- Peters, P. C., & Mathews, J. 1963, *Phys. Rev.*, 131, 435, doi: [10.1103/PhysRev.131.435](https://doi.org/10.1103/PhysRev.131.435)
- Pfahl, E., & Loeb, A. 2004, *Astrophys. J.*, 615, 253, doi: [10.1086/423975](https://doi.org/10.1086/423975)
- Poisson, E., & Will, C. M. 2014, *Gravity: Newtonian, Post-Newtonian, Relativistic* (Cambridge University Press), doi: [10.1017/CBO9781139507486](https://doi.org/10.1017/CBO9781139507486)
- Psaltis, D., Wex, N., & Kramer, M. 2016, *Astrophys. J.*, 818, 121, doi: [10.3847/0004-637X/818/2/121](https://doi.org/10.3847/0004-637X/818/2/121)
- Rea, N., et al. 2013, *Astrophys. J. Lett.*, 775, L34, doi: [10.1088/2041-8205/775/2/L34](https://doi.org/10.1088/2041-8205/775/2/L34)
- Reid, M. J., & Brunthaler, A. 2020, *Astrophys. J.*, 892, 39, doi: [10.3847/1538-4357/ab76cd](https://doi.org/10.3847/1538-4357/ab76cd)
- Reynolds, C. S. 2014, *Space Sci. Rev.*, 183, 277, doi: [10.1007/s11214-013-0006-6](https://doi.org/10.1007/s11214-013-0006-6)
- . 2019, *Nature Astron.*, 3, 41, doi: [10.1038/s41550-018-0665-z](https://doi.org/10.1038/s41550-018-0665-z)
- Riaz, S., Ayzenberg, D., Bambi, C., & Nampalliwar, S. 2020, *Astrophys. J.*, 895, 61, doi: [10.3847/1538-4357/ab89ab](https://doi.org/10.3847/1538-4357/ab89ab)
- Schoedel, R., et al. 2024, arXiv e-prints, doi: [10.48550/arXiv.2406.04022](https://doi.org/10.48550/arXiv.2406.04022)
- Shannon, R. M., & Cordes, J. M. 2010, *Astrophys. J.*, 725, 1607, doi: [10.1088/0004-637X/725/2/1607](https://doi.org/10.1088/0004-637X/725/2/1607)
- Shao, L., & Hu, Z. 2025. <https://arxiv.org/abs/2508.09931>
- Shapiro, I. I. 1964, *Phys. Rev. Lett.*, 13, 789, doi: [10.1103/PhysRevLett.13.789](https://doi.org/10.1103/PhysRevLett.13.789)
- Shklovskii, I. S. 1970, *Soviet Ast.*, 13, 562
- Stairs, I. H., Thorsett, S. E., & Arzoumanian, Z. 2004, *Phys. Rev. Lett.*, 93, 141101, doi: [10.1103/PhysRevLett.93.141101](https://doi.org/10.1103/PhysRevLett.93.141101)
- Taylor, J. H., Fowler, L. A., & McCulloch, P. M. 1979, *Nature*, 277, 437, doi: [10.1038/277437a0](https://doi.org/10.1038/277437a0)
- Thorne, K. S. 1980, *Rev. Mod. Phys.*, 52, 299, doi: [10.1103/RevModPhys.52.299](https://doi.org/10.1103/RevModPhys.52.299)
- Thrane, E., & Talbot, C. 2019, *Publ. Astron. Soc. Austral.*, 36, e010, doi: [10.1017/pasa.2019.2](https://doi.org/10.1017/pasa.2019.2)
- van Haasteren, R., & Levin, Y. 2013, *Mon. Not. Roy. Astron. Soc.*, 428, 1147, doi: [10.1093/mnras/sts097](https://doi.org/10.1093/mnras/sts097)
- Waisberg, I., et al. 2018, *Mon. Not. Roy. Astron. Soc.*, 476, 3600, doi: [10.1093/mnras/sty476](https://doi.org/10.1093/mnras/sty476)
- Wex, N. 1995, *Class. Quant. Grav.*, 12, 983, doi: [10.1088/0264-9381/12/4/009](https://doi.org/10.1088/0264-9381/12/4/009)
- Wex, N., & Kopeikin, S. 1999, *Astrophys. J.*, 514, 388, doi: [10.1086/306933](https://doi.org/10.1086/306933)
- Zhang, F., & Saha, P. 2017, *Astrophys. J.*, 849, 33, doi: [10.3847/1538-4357/aa8f47](https://doi.org/10.3847/1538-4357/aa8f47)